

Synthesis and Optical Ignition of Aluminum and Silicon-based
Energetic Materials

A DISSERTATION
SUBMITTED TO THE DEPARTMENT OF MECHANICAL ENGINEERING
AND THE COMMITTEE ON GRADUATE STUDIES
OF STANFORD UNIVERSITY
IN PARTIAL FULFILLMENT OF THE REQUIREMENTS
FOR THE DEGREE OF
DOCTOR OF PHILOSOPHY

Yuma Ohkura

October 2013

© 2013 by Yuma Ohkura. All Rights Reserved.

Re-distributed by Stanford University under license with the author.



This work is licensed under a Creative Commons Attribution-Noncommercial 3.0 United States License.

<http://creativecommons.org/licenses/by-nc/3.0/us/>

This dissertation is online at: <http://purl.stanford.edu/yw312xw5478>

I certify that I have read this dissertation and that, in my opinion, it is fully adequate in scope and quality as a dissertation for the degree of Doctor of Philosophy.

Xiaolin Zheng, Primary Adviser

I certify that I have read this dissertation and that, in my opinion, it is fully adequate in scope and quality as a dissertation for the degree of Doctor of Philosophy.

Mark Brongersma

I certify that I have read this dissertation and that, in my opinion, it is fully adequate in scope and quality as a dissertation for the degree of Doctor of Philosophy.

Alberto Salleo

Approved for the Stanford University Committee on Graduate Studies.

Patricia J. Gumport, Vice Provost for Graduate Education

This signature page was generated electronically upon submission of this dissertation in electronic format. An original signed hard copy of the signature page is on file in University Archives.

Abstract

Energetic materials, aluminum (Al) and silicon (Si), due to their large volumetric energy densities, earth abundance, and low cost, have broad applications in propulsion, thermal batteries, waste disposal and power generation for microsystems. The energetic materials are commonly prepared by mixing fuel and oxidizer powders, however, the energy release rates are slow and difficult to ignite. Furthermore, the large portion of the reactants remains unburned due to the formation of the oxide layer during the reaction. Optimized energetic materials would have the reactive components mixed on a scale as fine as possible to reduce the mass transport distance and facilitate the ignition. This leads to the idea of reducing the sizes of energetic materials down to nanoscale to increase the surface area and contact area between the fuel and oxidizer. In this study, we investigated two new areas: 1) the effects of the nanostructured morphology on the exothermic reaction of Al and CuO, 2) demonstrate and understand the flash ignition of Al nanoparticles (NPs), and extending the flash ignition to Al microparticles (MPs) and porous Si.

First, it remains a challenge to create energetic materials, a mixture of Al and metal oxides, with nanoscale uniformity. Here, we report synthesis and ignition studies on thermites (mixtures of Al and metal oxides) with unique nanostructures, i.e., CuO/Al core/shell nanowires (NWs) and Al/CuO core/shell micro and nano particles. The CuO NW cores were synthesized by the thermal annealing of copper films and

served as templates for the deposition of Al shells by subsequent sputtering. Similarly, for core/shell particles, the Al particles were coated with a very thin CuO shell using a solution phase method. The advantage of such core/shell structures are that CuO and Al are uniformly mixed at the nanoscale with no aggregation. The onset temperatures of the exothermic reaction of the core/shell NWs were similar to those of nanoparticle NP-based thermites in terms of magnitude, and insensitivity to equivalence ratios. Moreover, the core/shell NW thermites, compared to NP-based thermites, exhibit greatly improved mixing uniformity and reduced activation energy for the thermite reaction. For Al/CuO core/shell particles, in comparison to mixtures of Al particles and CuO NPs, have better chemical homogeneity and physical contact between Al and CuO, so that the core/shell particles exhibit much larger burning rates. The core/shell structure is a general and effective structure to tailor the combustion performance of energetic materials.

Second, nonintrusive optical flash ignition is attractive for many applications due to its simplicity, and flexibility in controlling the area exposed to the flash. However, the oxidation mechanism of Al NPs at large heating rates remains inconclusive due to the lack of direct experimental evidence. We studied the oxidation mechanism of Al NPs under large heating rate (on the order of 10^6 K/s or higher) by a simple flash ignition method, which uses a xenon flash to ignite Al NPs. The flash ignition occurs when the Al NPs have suitable diameters and sufficient packing density to increase the temperature above their ignition temperatures. We then

extended the flash ignition to Al MPs. Flash ignition of Al MPs is challenging due to their higher minimum flash ignition energy, which originates from weaker light absorption and higher ignition temperature compared to Al NPs. By the addition of WO₃ NPs to Al MPs, the minimum flash ignition energy of Al MPs was reduced and we studied the roles of WO₃ NPs upon flash ignition. Finally, we demonstrate that freestanding porous Si films can also be optically ignited in ambient air by a xenon flash. Our complementary experimental and numerical studies reveal that the minimum flash ignition energy increases with increasing the thickness due to heat loss through the porous Si layer. The minimum flash ignition energy is lower for higher porosity Si film since higher porosity reduces the heat capacity and thermal conductivity, facilitating the temperature rise. We believe that these results will be of great importance to reliably ignite energetic materials and to prevent unwanted combustion for practical energetic applications.

Acknowledgement

I would like to express my deep appreciation to my research advisor, Prof. Xiaolin Zheng, for her generous guidance, support and encouragement throughout my Ph.D. program at Stanford. She was constantly available for scientific discussions, and she is definitely one of my greatest role models as a professor. Her continuous and ambitious working attitude will always remind me the importance to work hard to overcome my future challenges in my career. I would like to thank her for teaching me the importance of writing/presentation skills, and for strongly cheering me throughout my Ph.D. program. I feel very fortunate to have Prof. Xiaolin Zheng as my advisor.

I would also like to thank, Prof. Mark Brongersma, Prof. Alberto Salleo, Prof. Tom Bowman and Prof. Debbie Senesky for serving as my defense committee. Their comments and suggestions at my defense encouraged me to think deeper and provided me a different perspective towards my research. In particular, I would like to thank Prof. Mark Brongersma and Prof. Alberto Salleo for their time reading my thesis.

I gratefully appreciate all the group members in the Zheng Research Group for their generous support. Dr. Dong Rip Kim, Dr. Yunzhe Feng, Dr. Pratap Rao, Dr. Chi Hwan Lee, Dr. Jeffery Weisse, Dr. In Sun Cho, and Dr. Hong Li gave me very

valuable feedback on my research and presentations. I also thank Shih-Yu Liu, Lili Cai, Runlai Luo. Working with them was one of my best moments in my academic life.

I would like to acknowledge the supportive Stanford lab staff members as well. Especially, Bob Jones for his assistance in SEM-EDS, Lakhbir Johal for machining my experimental parts, and Dr. Guangchao Li for running the ICP measurements.

I gratefully acknowledge the financial support from the Japan Student Service Organization for supporting my tuition and living expenses. Without the financial support, I would not be able to afford to study at Stanford University.

Last but not least, I would like to thank my parents and sister for their financial and mental support. I would not be able to progress through my Ph.D. degree without their help. I really cannot thank them enough for their continuous support.

Table of Contents

1. Introduction	1
1.1. Definitions and motivations.....	1
1.2. Background on nanoenergetics	2
1.2.1. Materials for nanoenergetics	2
1.2.2. The size dependence on the combustion and ignition of Al.....	3
1.2.3. Non-diffusional combustion mechanism: Melt-Dispersion Mechanism	10
1.2.4. Ignition and combustion studies on porous Si.....	11
1.2.5. The effect of morphology and porosity on burning rate of porous Si	13
1.3. Opportunities and challenges.....	15
1.4. Objectives and organization of the thesis	16
2. Synthesis of energetic materials: CuO/Al core/shell nanowires, Al/CuO core/shell particles, and porous Si film.....	18
2.1. Background on core/shell nanoscale thermites.....	18
2.2. Background on hydrogenated porous Si energetics.....	20
2.3. Synthesis and characterization of core/shell structured materials	22
2.3.1. Synthesis and characterization of CuO/Al core/shell nanowires	22
2.3.2. Synthesis and characterization of Al/CuO core/shell particles	25
2.4. Synthesis of freestanding porous Si film	29

2.5.	Conclusion	31
3.	Enhanced exothermic reaction of core/shell structured materials	32
3.1.	Experimental specifications	32
3.1.1.	Differential scanning calorimetry	32
3.1.2.	X-ray diffraction analysis	34
3.1.3.	Burning rate measurement.....	35
3.2.	Exothermic reaction of CuO/Al core/shell nanowires	36
3.2.1.	Effect of the Al layer thickness	36
3.2.2.	Effect of heating rate	38
3.2.3.	Comparison of nanowire- and nanoparticle-based thermites	41
3.3.	Enhanced combustion of Al/CuO core/shell particles	44
3.3.1.	Effect of structure on the onset temperature.....	45
3.3.2.	Effect of the core/shell structure on the burning rates.....	46
3.4.	Conclusion	47
4.	Flash ignition of Al particles and addition of WO ₃ nanoparticles.....	49
4.1.	Background.....	49
4.2.	Experimental specifications	50
4.2.1.	Flash ignition experimental setup.....	50
4.2.2.	Material preparation of Al nanoparticles and mixtures of Al microparticles/WO ₃ nanoparticles.....	52

4.3.	Flash ignition of Al particles	54
4.4.	Material characterization of Al and WO ₃ particles.....	56
4.4.1.	X-ray diffraction characterization of products of Al MPs and WO ₃ NPs	
	56	
4.5.	Estimation of the temperature increase of single and multiple Al particles ..	57
4.5.1.	Estimation of the temperature increase of single Al particles	57
4.5.2.	Estimation of the temperature increase of multiple Al particles	59
4.6.	Al nanoparticle oxidation mechanism	61
4.7.	Reducing minimum flash ignition energy of Al microparticles by addition of WO ₃ nanoparticles	65
4.7.1.	Minimum flash ignition energy of the mixture of Al MPs and WO ₃ NPs	
	65	
4.7.2.	Optical characterizations of Al MPs with addition of WO ₃ nanoparticles	
	66	
4.8.	Conclusion	68
5.	Flash ignition of freestanding porous Si film	70
5.1.	Background.....	70
5.2.	Flash ignition of porous Si film	71
5.2.1.	Experimental setup and flash ignition process of Si film.....	71
5.2.2.	Minimum flash ignition energy of porous Si film.....	73

5.2.3. Estimation of the temperature increase of a porous Si film	75
5.3. Conclusion	82
6. Conclusion.....	83
7. Recommendation for future work	86
7.1. Oxidation kinetics studies of thermite mixtures using the Micro-Thermal Stage	86
7.2. Engineering application of flash ignition: Airbag igniter	89
8. Bibliography	91

List of Tables

Table 1: The effect of film thickness on burning rate. [24].....	13
Table 2: The effect of porosity on burning rate. [24]	14
Table 3: Parameters and values of porous Si used in the COMSOL simulation.....	78

List of Figures

Figure 1-1: Gravimetric and volumetric heat of oxidation of inorganic energetic materials. [2].....	3
Figure 1-2: Schematic representation of the flame structures observed in aluminum combustion. [6].....	4
Figure 1-3: Experimental data of Al particle burning time as a function of particle diameter. [7]	6
Figure 1-4: The Al size effect on ignition temperatures. [8].....	6
Figure 1-5: Phase change process of the Al particle surface with respect to temperature and TGA curve. [9].....	8
Figure 1-6: Ignition temperature predicted by multiple aluminum oxide polymorphs model as a function of particle size. [12]	9
Figure 1-7: Schematic of non-diffusional combustion mechanism: Melt-Dispersion Mechanism. [13].....	10
Figure 1-8: Schematic of the initiation of explosive reaction between the hydrogenated porous Si and cryogenic oxygen. [22]	12
Figure 2-1: (a) The reaction pathways of porous Si formation etching and electropolishing. (b) The lift-off mechanism for undercutting of a porous Si layer. [56]	21
Figure 2-2: a) Schematics of the fabrication process of the CuO/Al core/shell NWs. The insets are the corresponding optical images. SEM images of the b) CuO NWs, c)	

CuO/Al (250 nm) core/shell NWs, and d) enlarged view of c). The yellow dashed lines outline each core/shell nanowire.	22
Figure 2-3: Effect of the growth time on the morphology of the CuO NWs annealed at 500 °C. SEM images of NWs grown for a) 5 hours and b) 24 hours. The inset shows that the CuO NWs are connected to the underneath CuO layer.	24
Figure 2-4: a) Schematics of the synthesis process of the Al/CuO core/shell particles. TEM images of the b) initial Al particles, c) Al/CuO core/shell particle, and d) enlarged view of c).	26
Figure 2-5: a) TEM image of the Al/CuO core/shell MP. b) and c) EDS elemental mapping images of Cu and O.	28
Figure 2-6: (a) Cross-sectional schematic of an anodization cell used for the porous Si formation, and electropolishing. [63] (b) Cross-sectional SEM image of the porous Si layer formed over the Si wafer.	30
Figure 3-1: The DSC calibration curve measuring the heat of fusion of KBr (56.85 mg). The integrated area under the heat of fusion curve is 51.956 μ Vs/g.	33
Figure 3-2: Parallel beam XRD of CuO/Al (250nm) core/shell NWs a) before and b) after the DSC test.....	34
Figure 3-3: a) Schematic and b) optical image of the microchannel device for burning rate measurement. The thermite reaction propagates across the microchannel associated with the visible emission, which was collected by the photo-diode through an equally-spaced array of optical fibers.....	35

Figure 3-4: DSC traces for reactions of the CuO/Al core/shell NWs with different Al shell thickness (100 nm, 250 nm, and 425 nm). All the traces were recorded in inert He at a heating rate of 5 °C/min.	37
Figure 3-5: a) DSC traces for reactions of the CuO/Al (250nm) core/shell NWs at heating rates of 5 °C/min, 15 °C/min, 25 °C/min and 40 °C/min. b) The exothermic onset temperatures of the CuO/Al core/shell NWs at different heating rates.	39
Figure 3-6: Thermal analysis of DSC traces for the CuO/Al (250 nm) core/shell NWs, and CuO/Al NPs at equivalence ratios of 1.00 and 0.24.	40
Figure 3-7: Comparison of DSC traces for reactions of CuO/Al (425nm) core/shell NWs, a stoichiometric mixture of CuO NWs and Al NPs, and a stoichiometric mixture of CuO and Al NPs.	42
Figure 3-8: Comparison of DSC traces for reactions of Al/CuO core/shell (a) NPs and (b) MPs vs. mixtures of Al NPs and CuO NPs with same equivalence ratio ($\Phi = 6.3, 8.1$).	46
Figure 3-9: Photo-diode signal voltages as a function of time for Al/CuO core/shell (a) NPs and (b) MPs compared to Al/CuO powder mixtures at equivalent stoichiometry. The peak signal voltages are indicated by the reverse triangle and the burn rate is determined by dividing the distances between the five fiber-optic probes by the time delay of the peak voltages. (c) Comparison of burn rates of Al/CuO core/shell particles vs. mixture of Al particles (both NPs and MPs) and CuO NPs.	47
Figure 4-1: Pulse energy calibration with respect to the power setting of the xenon flash	51
Figure 4-2: Intensity of xenon flash spectrum with respect to wavelength.	51

Figure 4-3: (a) Schematic and (b) optical images of the experimental setup for ignition of Al NPs (80 nm) by a camera flash. Inset: photograph of the burning of flash ignited Al NPs which casts a yellow glow and lasts for about 10 s.	52
Figure 4-4: (a–c) Optical and SEM images of Al NPs before and after the exposure. The original spherical Al NPs break up into smaller clusters after burning. (d-f) Optical and SEM images of a mixture Al MPs (2.3 μm) and WO_3 NPs (80 nm). After the flash ignition, the products form much larger particles that are tens of microns in size, suggesting that melting and fusion occur together with reaction.	55
Figure 4-5: X-ray diffraction pattern of the mixture of Al MPs (2.3 μm) and WO_3 NPs (80 nm, $\phi = 1$, $\phi_n = 0.5$) after ignition.....	56
Figure 4-6: Estimated temperature rise of Al particles by a flash exposure as a function of the Al particle diameter for different packing densities. Inset: The temperature rise of Al NPs with a diameter of 70 nm as a function of the packing density of Al NPs..	60
Figure 4-7: Exposure of Al NPs to a flash in Ar. a) TEM image of the Al NPs before flash exposure. Inset: the Al NP is covered by an alumina shell about 2 nm thick. b) and c) TEM images of two different Al NPs after flash exposure in Ar showing that both alumina shells have ruptured after the flash exposure.	62
Figure 4-8: (a - e) Schematics and (f - i) TEM images illustrate the oxidation process of the Al NPs when exposed to a flash in the air. a) Initial Al NPs are covered by a Al_2O_3 shell. b) and f) Al melts upon rapid heating which pushes the shell outward. c) and g) the shell ruptures and the melted Al becomes in contact with air. d) and i) the large hollow sphere corresponds to the expanded Al NPs, where most Al has flown away from the particle center and been oxidized at the particle surface. e) and j), the	

hollow sphere fractures into small clusters of 3 – 20 nm in sizes. These clusters are consisted of both Al_2O_3 particles and partially oxidized Al particles.	64
Figure 4-9: Minimum flash ignition energy of Al MPs with addition of WO_3 NPs. a) Large Al MPs (2.3 μm) and b) small Al MPs (0.9 μm) mixed with WO_3 NPs with respect to normalized equivalence ratios in air and nitrogen gas.	66
Figure 4-10: Optical characterizations of Al MPs with addition of WO_3 NPs. Absorption a) large Al MPs (2.3 μm) and b) small Al MPs (0.9 μm) mixed with WO_3 NPs with respect to normalized equivalence ratios over a wavelength of 300 - 1100 nm.	67
Figure 5-1: (a) Schematic of the experimental setup for the ignition of freestanding porous Si films by a xenon flash. (b) Optical images of a freestanding porous Si film before and during the xenon flash exposure.	71
Figure 5-2: High speed camera images capturing the ignition and combustion process of a freestanding porous Si film when exposed to the xenon flash. The porous Si film ignites at multiple locations and the reaction front propagates from the ignition region into the unreacted porous Si regime.	72
Figure 5-3: Experimentally measured minimum flash ignition energies of freestanding porous Si films as functions of film thickness and porosity. The error bar represents the standard deviation of the E_{min}	75
Figure 5-4: Schematic of the numerical setup for calculating the temperature rise of a freestanding porous Si film by the xenon flash.	76
Figure 5-5: Calculated time-dependent temperature profile within the freestanding porous Si film.	78

Figure 5-6: Calculated maximum temperature rise of freestanding porous Si films by the xenon flash as functions of film thickness and porosity.....	79
Figure 5-7: Calculated minimum flash ignition energy density for freestanding porous Si films by the xenon flash as functions of film thickness and porosity.	81
Figure 7-1: Experimental schematic of the micro-thermal stage	87
Figure 7-2: A prototype of a porous Si based airbag igniter. [20]	90

1. Introduction

1.1. Definitions and motivations

Energetic materials are substances that store chemical energy and monomolecular compounds of energetic materials are of Trinitrotoluene (TNT), Research Department Explosive (RDX), High Melting Explosive (HMX), etc. [1] The monomolecular energetic materials react rapidly with the rate controlled by the chemical kinetics processes of the molecule decomposition. One of the limitations of the monomolecular energetic materials is that its relatively low energy density. Higher combustion energies and energy density materials (e.g., Al and Si) are gaining great research interest to overcome the low energy densities of monomolecular compounds. The traditional Al and Si energetic materials are produced by mixing oxidizers with fuel powders to produce composite energetic materials. These composites exhibit high energy density, but their energy release rates are slower than monomolecular material because the mass transport rate is controlled by relatively slow heterogeneous reactions and difficult to ignite. Furthermore, the large portion of the reactants remains unreacted, since the oxide layers form during the exothermic reaction and block the fuel to react with the oxidizer.

In view of the above considerations, optimized energetic material would have the reactive components mixed on a scale as fine as possible to reduce the mass

transport distance and facilitate the ignition. This leads to the idea of using materials with high specific surface area, or materials divided down to the nano-scale in order to reduce ignition delays and accelerate combustion of energetic materials. These nano-scale energetic materials are often referred to as “nanoenergetics”.

The motivation of this dissertation is twofold: 1) to develop a nanostructure that scales down both fuel and oxidizer in an efficient united structure, and compare the combustion characteristics with the conventional powder structure 2) to demonstrate a reliable xenon flash ignition method to energetic materials and understand the mechanism of flash ignition.

1.2. Background on nanoenergetics

1.2.1. Materials for nanoenergetics

The material candidates for nanoenergetics with high energy densities are illustrated in Figure 1-1. [2] Monomolecular compounds such as TNT and RDX have gravimetric and volumetric energy densities of 15 kJ/g, 24.8 kJ/cm³ and 9.5 kJ/g, 17.4 kJ/cm³, respectively. [3] From Figure 1-1, Al and Si have higher gravimetric energy densities of 31.1 kJ/g, and 32.4 kJ/g than TNT and RDX. Furthermore, the advantage of using Al and Si becomes more significant when comparing the volumetric energy densities of 83.8 kJ/cm³, 80.1 kJ/cm³. [4] Other advantages of Al and Si are their high combustion temperature (up to 3250K), environmentally benign products. Due to the advantages described above, Al and Si are great candidates for the nanoenergetic

materials. From the energy density perspective, other materials such as Boron (B) and Beryllium (Be) are also attractive candidates for the nanoenergetics. However, Si and Al are the 2nd and 3rd abundant elements in Earth's crust and it is this earth abundance that makes Si and Al the desirable candidates for nanoenergetic materials.

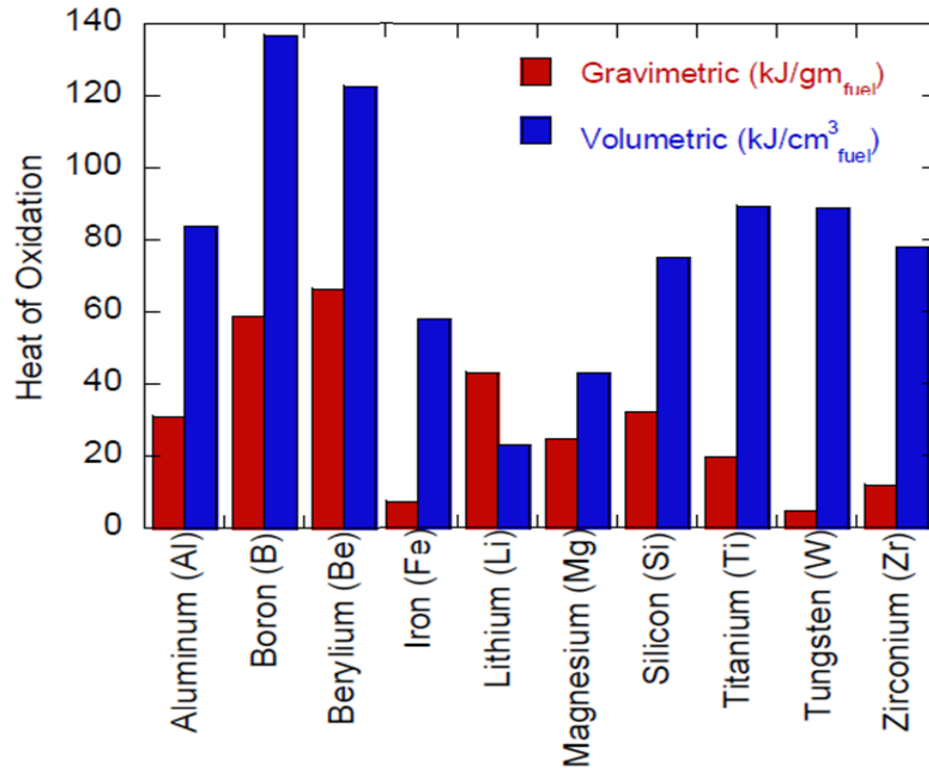


Figure 1-1: Gravimetric and volumetric heat of oxidation of inorganic energetic materials. [2]

1.2.2. The size dependence on the combustion and ignition of Al

Aluminum combustion has been studied from relatively large particles ($> 10 \mu\text{m}$) down to small particles ($< 1 \mu\text{m}$) and decreasing particle size leads to faster

combustion and enhances the performance of propellants. [5] As the particle size becomes smaller, the particle flame structure will deviate from the vapor-phase diffusion flame and transition to kinetic-limited combustion. The burning behavior of the transition from diffusion-limited to kinetic-limited combustion is illustrated in Figure 1-2. [6] For large ($> 50 \mu\text{m}$) aluminum particle combustion, models and empirical relations have been developed to describe the combustion behavior based on the vapor-phase diffusion combustion. The burn time fits to the power law relation with an exponent typically slightly below two due to oxide accumulation on the Al surface. (Figure 1-3) The detached vapor-phase diffusion flame forms a few radii from the particle surface where the Al and oxidizer react. The temperature peaks in the flame region and the size at which the flame structure transitions from the vapor-phase diffusion flame is around $10 \mu\text{m}$ in the environment of 50% O_2 and 50% Ar. [6]

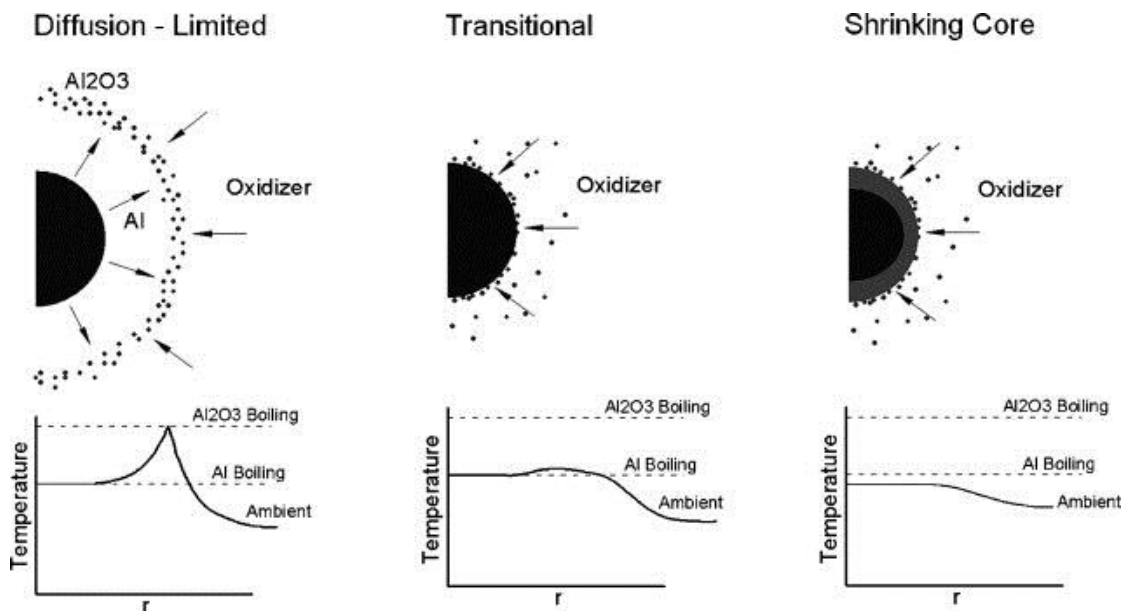


Figure 1-2: Schematic representation of the flame structures observed in aluminum combustion. [6]

The transitional combustion state from diffusion-limited to kinetic-limited demonstrates the near surface-limited combustion process. As particle becomes smaller, diffusion becomes faster, and the flame moves closer to the Al particle surface. The reactions occur in the gas-phase very near the particle surface. Since the flame moves closer to the particle surface, the Al particle acts as a heat sink for the energy released during the exothermic reaction. The peak temperature occurs near the particle surface, and the temperature remains near the aluminum boiling temperature (2791 K). As the Al particle become below 10 μm , the aluminum combusts in the condensed-phase via the shrinking core model. The oxidizer diffuses onto the particle surface and through the alumina oxide layer and the combustion temperature is the highest within the particle. In summary, studies on burning time [7] and flame temperature measurements [6] agree well with the size dependence on the Al combustion mechanisms, thus, by varying the Al particle size, one could control the Al combustion performances.

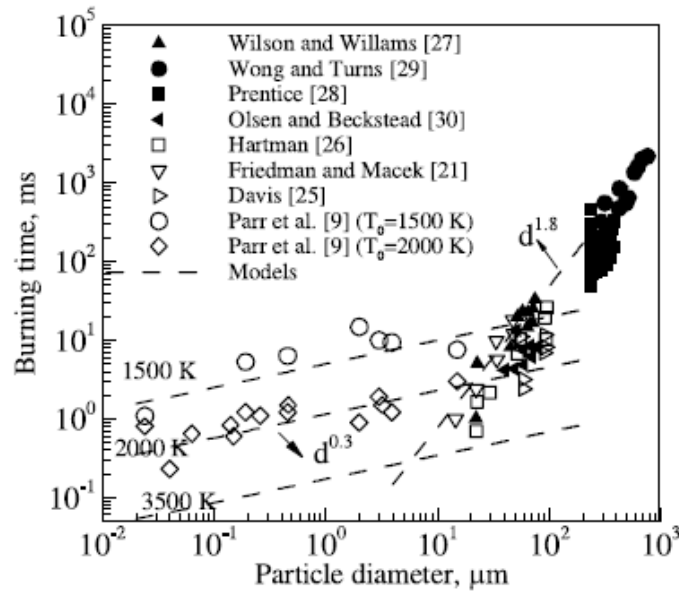


Figure 1-3: Experimental data of Al particle burning time as a function of particle diameter. [7]

Besides the burning time and flame temperature, the ignition temperature is also a strong function of the Al particle size. The ignition temperatures of Al as a function of the size is shown in Figure 1-4.

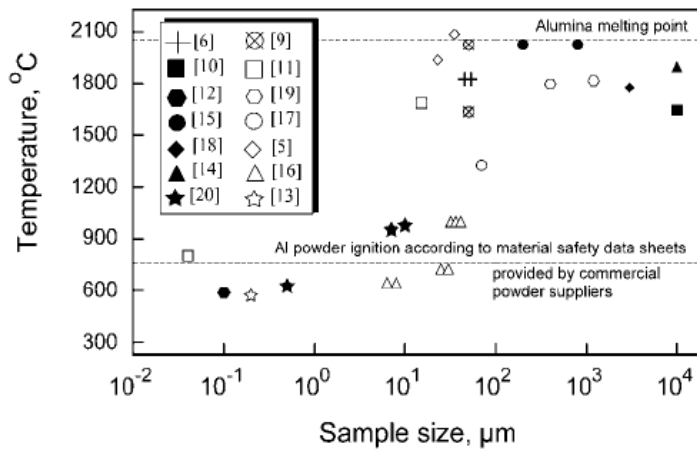


Figure 1-4: The Al size effect on ignition temperatures. [8]

As the sample size decreases, the Al ignition temperature also decreases. Currently, there are several ignition models reported for Al ignition to explain this trend. Here, we introduce two ignition models: 1) Fixed ignition temperature and 2) multiple aluminum oxide polymorphs.

1) Fixed ignition temperature

The fixed ignition temperature model is applicable to large Al sizes ($> 50 \mu\text{m}$). For large Al sample sizes, Figure 1-4 indicates that Al ignites close to the melting point of Al_2O_3 (2053°C). This suggests that once the passivation of the oxide film is melted, the core Al is exposed to air leading to ignition.

2) Multiple aluminum oxide polymorphs

The second model, which is an extension of the fixed ignition temperature model, was developed to explain the size dependence of the Al ignition temperature. [9, 10] During the thermal oxidation, the growth of the passivation layer of alumina is associated with phase transformations. The phase transformations at different stages lead to discontinuities in the oxide layer altering the diffusion and oxidation rate by the surrounding gaseous oxygen. Based on the kinetic relations (i.e., activation energies, pre-exponents) of the polymorphic phase changes and heat transfer analysis, the surface temperature of the particle exceeds the Al_2O_3 melting point at different sizes as a result of self-heating during different oxidation stages. The entire oxidation and phase change process is illustrated in Figure 1-5. The initial amorphous film goes through the transformation from amorphous Al_2O_3 , $\gamma\text{-Al}_2\text{O}_3$, $\delta\text{-Al}_2\text{O}_3$, $\theta\text{-Al}_2\text{O}_3$ to $\alpha\text{-Al}_2\text{O}_3$. The

densities of the alumina polymorphs increases as the phase transforms from amorphous Al_2O_3 to $\alpha\text{-Al}_2\text{O}_3$ (3 g/cm^3 to 4 g/cm^3). This density transition would cause discontinuities in the oxide layer during the oxidation.

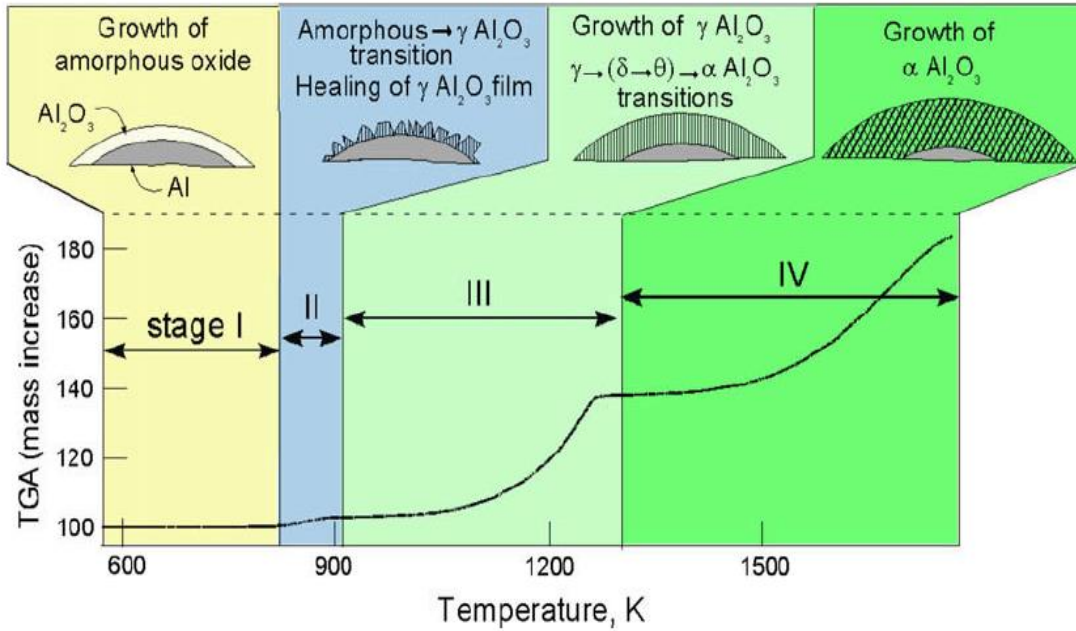


Figure 1-5: Phase change process of the Al particle surface with respect to temperature and TGA curve. [9]

Once the thermal oxidation takes place between the temperature range of 20 – 600 °C, the amorphous Al_2O_3 film grows above the critical stable thickness and transitions to $\gamma\text{-Al}_2\text{O}_3$. In higher temperature regime (950 – 1250 °C), $\gamma\text{-Al}_2\text{O}_3$ transforms in the order of $\delta\text{-Al}_2\text{O}_3$, $\theta\text{-Al}_2\text{O}_3$ to $\alpha\text{-Al}_2\text{O}_3$. The ratio of the heat release due to oxidation over the particle heat capacity depends on the particle size because

smaller particles self-heat more efficiently. [8, 10, 11] From this model, nano-scale particles ($< 1 \mu\text{m}$) ignite at lower temperatures, when the continuity of the amorphous oxide layer is disrupted as a result of the formation of $\gamma\text{-Al}_2\text{O}_3$. From particle size of $1 \mu\text{m}$ to $25 \mu\text{m}$, the phase change from $\gamma\text{-Al}_2\text{O}_3$ to $\alpha\text{-Al}_2\text{O}_3$ occurs and the rapid oxidation continues because of the gaseous oxygen diffusion to the exposed Al surface leading to ignition. The proposed model (solid line in Figure 1-6) of Al ignition predicts the effect of the particle size on ignition temperatures, which is consistent with other experimental data.

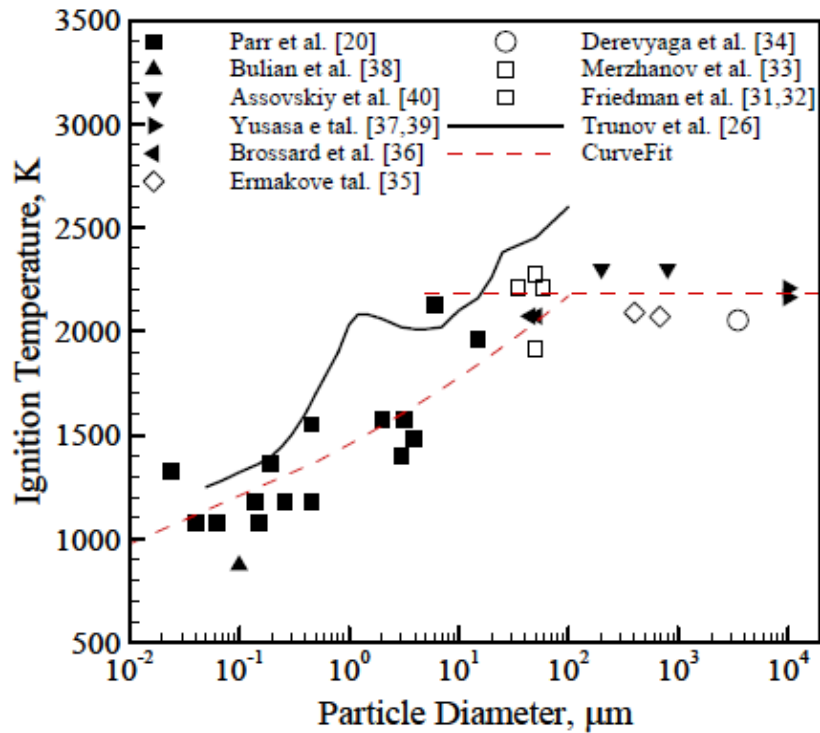


Figure 1-6: Ignition temperature predicted by multiple aluminum oxide polymorphs model as a function of particle size. [12]

1.2.3. Non-diffusional combustion mechanism: Melt-Dispersion Mechanism

Recently, numerous studies on Al NPs combustion have been conducted, and a new non-diffusional ignition and combustion mechanism: Melt-Dispersion Mechanism (MDM) has been proposed. [13] The schematic of the MDM process is illustrated in Figure 1-7.

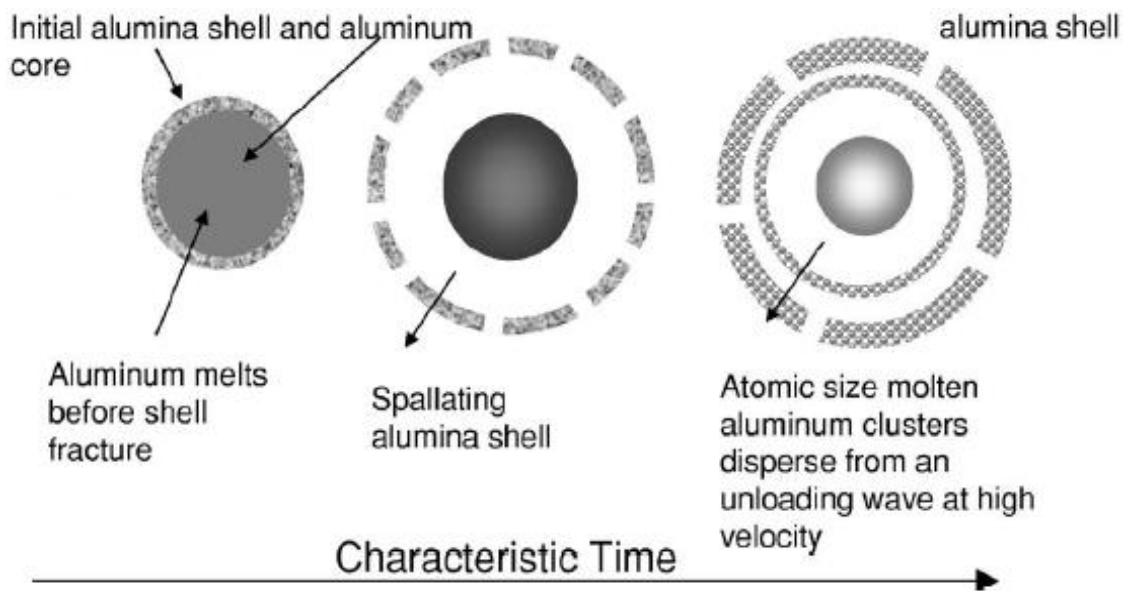


Figure 1-7: Schematic of non-diffusional combustion mechanism: Melt-Dispersion Mechanism. [13]

MDM typically occurs for Al NPs at large heating rates (i.e., $10^6 - 10^8$ K/s), and assumes that the volume increase due to the melting of Al creates a large pressure rise within the NP. The high pressure within the NP ruptures the Al_2O_3 shell and generates a

pressure wave that propagates to the center of the particle and disperses the molten Al into small clusters. MDM is not limited by diffusion and the flame propagation rate and the ignition time delay are independent of the radius. [14-17] According to the elasticity theory, the geometric parameter that determines stresses in the Al/Al₂O₃ core/shell system is $M = R/\delta$, the ratio of Al core radius R to oxide thickness δ . When $M < 19$, the whole core Al melts before the oxide fracture, which is the condition to trigger the MDM. The MDM is proposed to occur for nanoscale particles ($M < 19$), unless the oxide shell is pre-stressed or increased by thermal treatment prior to the ignition. However, no direct experimental observation has been reported to confirm the MDM.

1.2.4. Ignition and combustion studies on porous Si

In addition to Al, porous Si is also a promising material for nanoenergetics, due to its large volumetric energy density (80.7 kJ/cm³) [18] and the compatibility to integrate into Micro-Electro-Mechanical Systems (MEMS) such as accelerometers [19] and airbag initiators [20] to produce heat, gas, and control delivery pressures. [21] In 2001, porous Si was found to explode at temperatures as low as 4.2 K in cryogenic oxygen by Kovalev *et al.* [22] They reported the three step initiation mechanism of explosive reaction between the porous Si and cryogenic oxygen (Figure 1-8).

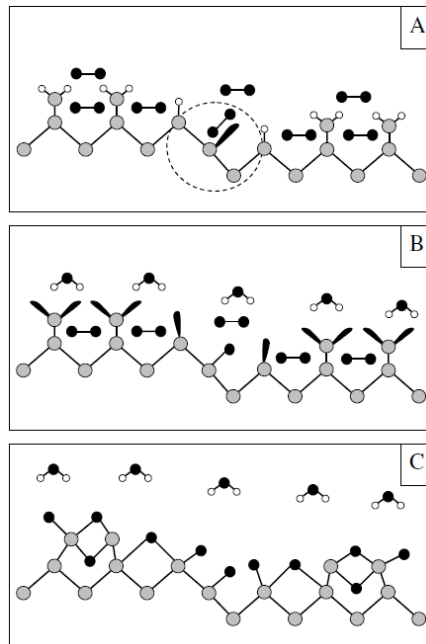


Figure 1-8: Schematic of the initiation of explosive reaction between the hydrogenated porous Si and cryogenic oxygen. [22]

In Figure 1-8A, hydrogen atoms cover the porous Si surface to block between Si atoms and oxygen. Nevertheless, a small number of Si dangling bonds do exist and the dashed circle indicates the dangling bond of Si, which is the ignition site. To advance to the explosive oxidation, hydrogen atoms are ruptured by energy transfer to nearby Si-H_x sites. This rupture process is accompanied by the exothermic reaction of oxygen and hydrogen, which forms water or OH radicals (Figure 1-8B). The removal of hydrogen atoms leads to new radical formation. Surface Si atoms react with oxygen, and the ignition and oxidation of Si are accomplished (Figure 1-8C). The reaction creates new radicals such as Si dangling bonds, atomic hydrogen and oxygen, or OH groups, hence,

the porous Si leads to explosive reaction. The separation of hydrogenated bonds on the porous Si surface in the air is reported to be around 300 °C. [23]

1.2.5. The effect of morphology and porosity on burning rate of porous Si

The burning rate of the porous Si impregnated with oxidizers (e.g., NaClO₄, Mg(ClO₄)₂) varies with film thickness, micro-structures, and porosity. The burning rate is strongly influenced by the confinement due to the gaseous reaction products. Increasing the thickness of the porous Si film filled with NaClO₄ enhances the confinement within the depths of the pores leading to increasing the burning rate from 2.4 m/s up to 400 m/s shown in Table 1. [24]

Table 1: The effect of film thickness on burning rate. [24]

Pore depth [μm]	Velocity confined [m s ⁻¹]
4.2 ± 0.2	2.4 ± 0.8
8.8 ± 0.1	3.8 ± 0.7
14.4 ± 0.4	19 ± 6
26.2 ± 0.2	27.6 ± 7.0
42.9 ± 0.4	324 ± 45
53.7 ± 0.6	425 ± 96
72.0 ± 0.6	399 ± 124

In addition to the film thickness, the microstructures patterned on the porous Si layer play an important role in the burning rate. Parimi [25] fabricated porous micro-

pillars using microfabrication techniques on the porous Si layer ($\sim 170 \mu\text{m}$) infused with magnesium perchlorate ($\text{Mg}(\text{ClO}_4)_2$). The porous micro-pillar structure exhibited burning rate up to 500 m/s, while the non-patterned porous Si film only demonstrated 1 - 8 m/s. Both studies indicate that burning rate can be controlled by porous Si morphology (film thickness and structural modifications). Alternatively, the porosity could also control the burning rate of the porous Si film. The burning rate experiments reported have validated that the burning rate increases as the porosity increases. (Table 3) In summary, studies have revealed that the thickness, microstructure, and porosity of porous Si have significant effects on the burning rate. By tailoring the morphology and porosity, one can adjust the combustion characteristics of porous Si for their specific energetic applications.

Table 2: The effect of porosity on burning rate. [24]

Porosity [%]	Velocity unconfined [m s ⁻¹]
69.7 ± 0.6	334 ± 68
64.7 ± 0.5	276 ± 70
60.0 ± 0.1	231 ± 45
58.1 ± 2.1	124 ± 7
52.3 ± 1.3	103 ± 13

1.3. Opportunities and challenges

In previous literature, the majority of the studies has focused on scaling down the size of the fuel and oxidizer independently. For instance, authors have reported [26] that pure Al NPs based propellant combined with Ammonium Perchlorate has unstable and no reproducible combustion characteristics because of the difficulty in uniformly mixing the ultrafine Al particles into the propellant. Weismiller [27] verified that the dimension of the oxide particles have a stronger influence on the burning rate of the thermite reaction than that of the of fuel particles. The burning rate was further enhanced with the nanoscale oxidizer due to shorter heat-up times and smaller gas diffusion length. Moreover, Rossi [21] stated that the fuel and oxidizer ought to have the same scale size to obtain the optimum high thermal diffusivity for bilayer material structure. However, very few studies have been focused on uniformly distributing the fuel and oxidizer in a combined structure. Hence, there is a great opportunity to synthesize a nanostructure that would scale down both fuel and oxidizer in an efficient united structure, and further compare the combustion characteristics with the conventional NP structure.

Another opportunity is to study and develop a reliable ignition method for nanoenergetics. Al and Si are difficult to ignite due to the high ignition temperatures. Moreover, the combustion of the nanoenergetics in MEMS encounters a large heat loss through the surrounding walls, which leads to ignition failures. There is demand is to minimize heat losses and achieve reliable ignition, which is one of the most challenging

issues to be solved for Al and Si energetics. A number of studies [19, 20, 28-31] have demonstrated various ways to implement nanoenergetics into engineering applications, however, not enough effort has been devoted to study and characterize non-conventional ignition methods.

1.4. Objectives and organization of the thesis

The objectives of the thesis are to identify and solve the opportunities and challenges described above. First, we report the synthesis and ignition studies on thermites with new core/shell nanostructures: 1) CuO/Al core/shell nanowires 2) Al/CuO core/shell particles. The advantage of such core/shell structure is that CuO and Al are uniformly mixed at the nanoscale. Second, we demonstrate and understand the flash ignition Al NPs, Al MPs, and porous Si films. The oxidation mechanism of flash ignition is revealed for Al NPs and the critical physical parameters that govern the flash ignition of the Al particles and porous Si are identified from both experiments and calculations.

The main body of the dissertation includes six chapters.

- Chapter 1 introduces the backgrounds of the nanoenergetics and the objectives of the thesis. By reviewing the current literature, we present that the combustion characteristics of Al and porous Si have a strong effect on the dimension and morphology.

- Chapter 2 presents the synthesis of energetic CuO/Al core/shell nanowires, Al/CuO core/shell particles and porous Si film. For CuO/Al core/shell nanowires, the CuO NWs were grown on Cu substrates with the thermal annealing method, and a conformal layer of Al was subsequently deposited over the CuO NWs by magnetron sputtering. For Al/CuO core/shell particles, the Al particles were coated with a very thin CuO shell using a solution phase method. Both core/shell NW-based and particles-based Al/CuO composite were synthesized to demonstrate the excellent chemical homogeneity. For porous Si film, electrochemical etching and electropolishing are conducted on a Si wafer to synthesize the freestanding porous Si film.
- Chapter 3 examines the enhanced exothermic reaction of core/shell structured materials. The core/shell structure materials exhibited small or no endotherm of Al melting compared to the powder mixture suggesting that the increase in the contact area enhances the fuel utilization of Al.
- Chapter 4 and 5 introduces the flash ignition of Al particles, and porous Si film. Chapter 4 demonstrates and understands the flash ignition of Al NPs, and MPs by the addition of WO₃ NPs. We identify the requirements for successful flash ignition and investigate the role of WO₃ NPs upon flash ignition. Chapter 5 extends the flash ignition to freestanding porous Si film. We discuss the important parameters that control the minimum flash ignition energy of the porous Si film in ambient air.
- Chapter 6 summarized the thesis and presents a guideline for future research possibilities.

2. Synthesis of energetic materials: CuO/Al core/shell nanowires, Al/CuO core/shell particles, and porous Si film

In this chapter, we introduce the background and synthesis of energetic materials focused on two subjects: 1) the core/shell structure thermite, and 2) the hydrogenated porous Si freestanding film. We adopted the core/shell and porous structure to design the energetic material to have nanoscale chemical uniformity, and to increase the surface area for the larger reaction area.

2.1. Background on core/shell nanoscale thermites

The nanoscale thermites (or nano-thermites) can be produced by many methods which were summarized in recent reviews, [32-35] such as arrested reactive milling, [36-40] powder mixing, [41-44] self-assembly, [45, 46] and layered vapor deposition. [47, 48] However, all of these methods suffer from certain shortcomings. For instance, although the mechanical mixing of Al with metal oxide nanoparticles (NPs), such as direct mixing in an ultrasonic bath using hexane or isopropanol, [49] is simple, it cannot homogeneously mix Al and metal oxides with a large degree of spatial homogeneity due to aggregation of the same type of NPs. As such, these materials exhibit large scatter in their ignition and burning characteristics. Blobaum et al. [47, 50]

demonstrated a different method to form highly uniform CuO_x/Al multilayer foils by alternately depositing Al and copper oxide layers with well-defined thicknesses under high vacuum, but this fabrication process is costly, time-consuming and difficult to scale up. The above limitations have hindered the fundamental understanding and optimization of nano-thermites. Therefore, there is a critical need to develop new, simple and yet scalable methods to create well-defined thermites with nanoscale mixing and homogeneity for both fundamental studies and practical applications.

Recently, core/shell structured nano-energetic materials have been proposed as an ideal structure to assemble nano-thermites for improved mixing uniformity and increase the interfacial area between the fuel and oxidizer. One approach is to directly deposit a layer of Al film with controlled thickness on top of metal oxide NWs to form uniform metal oxide/Al core/shell NW thermites. [51, 52] However, studies have been mainly focused on the fabrication process for integration of the nano-thermites onto Si wafers for potential applications in microelectronic mechanical systems. Another approach is to coat metal oxide layers on Al NPs using atomic layer deposition (ALD). [53] The advantage of this approach is that the synthesized thermite results in a large reaction interface area in the form of powder, which is convenient to handle. It was reported that the SnO_2 -coated Al particles reacted much more quickly and violently than the uncoated Al particles. Few examples of the ideal core/shell structured nanoenergetic materials have been demonstrated, however, the fundamental ignition characteristics of these core/shell NW and core/shell particle thermites were not systematically studied. In view of the above considerations, we performed synthesis of the core/shell structured

nanoenergetic materials both core/shell NWs and particles to experimentally determine the ignition/heat release characteristics of the core/shell structured nanoenergetics.

2.2. Background on hydrogenated porous Si energetics

Porous Si is another promising nanoenergetic material that has a large volumetric energy density (80.7 kJ/cm^3) [18] over two times higher than that of TNT. In 2001, porous Si when filled with cryogenic oxygen was reported to spontaneously explode at temperatures as low as 4.2 K due to heterogeneous hydrogen-oxygen and silicon-oxygen branched chain reactions by Kovalev *et al.* [22]. This discovery has sparked great interests of using porous Si as nanoenergetic materials. In addition to low temperature reactivity, porous Si can rapidly release energy with a reported burning rate up to 3050 m/s. [19, 24, 25, 54] Moreover, porous Si can be conveniently integrated into Micro-Electro-Mechanical Systems (MEMS) such as accelerometers [19] and airbag initiators [20] to produce heat, gas, and control delivery pressures. [21] Hence, porous Si has emerged as a promising material for energetic and pyrotechnic applications and the basic properties of porous Si for pyrotechnic applications were thoroughly reviewed by Koch *et al.* [23] and Plessis. [55]

Freestanding porous Si films are typically synthesized by electrochemical etching of a bulk Si wafer followed by electropolishing. The electrochemical etching is conducted through anodizing the Si wafer in hydrofluoric acid (HF) solution using an anodizing cell. During the electrochemical process, a constant current density is

maintained between the Si wafer and platinum (Pt) cathode that is placed in the HF solution. The current supplies holes to the Si surface along the electric field created within the wafer. At the Si surface, holes break apart the Si-H bonds and forms Si-H, Si-O and Si-F bonds. [56] The Si-F bonds are highly polarized due to the high electronegativity, and additional holes and fluoride ions are attracted. Hence the Si atoms dissolve in water in the form of SiF_6^{2-} leading to the formation of the porous Si layer. Next, the electropolishing is achieved by increasing the current density. Under this condition, the transport rate of fluorine ions cannot sustain with the high injection rate of holes, and Si-O bonds start to generate. Subsequently, a continuous silicon oxide layer forms underneath the porous layer. Finally, the porous Si film liftoffs from the original Si wafer resulting in a freestanding porous Si film as the silicon oxide layer is under-etched with HF. The reaction pathway of electrochemical etching and electropolishing are displayed in Figure 2-1.

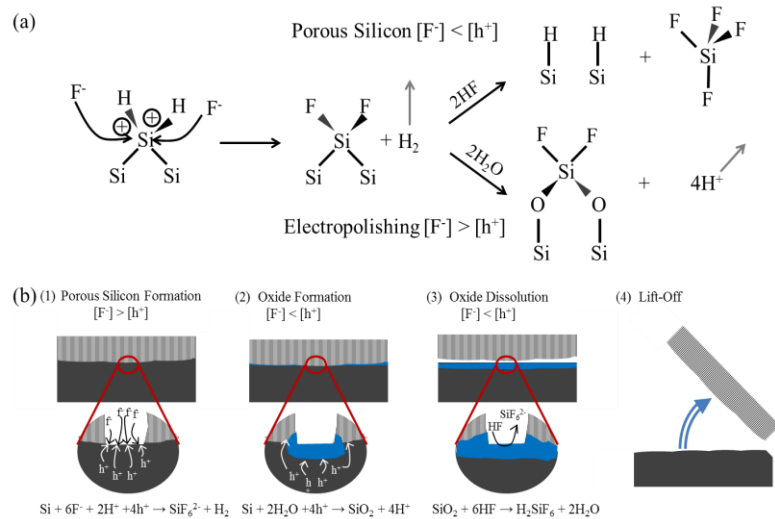


Figure 2-1: (a) The reaction pathways of porous Si formation etching and electropolishing. (b) The lift-off mechanism for undercutting of a porous Si layer. [56]

2.3. Synthesis and characterization of core/shell structured materials

2.3.1. Synthesis and characterization of CuO/Al core/shell nanowires

We have synthesized CuO/Al core/shell NWs by the thermal annealing of electroplated Cu film to grow CuO NWs, followed by Al film deposition by sputtering. The fabrication process of the CuO/Al core/shell NWs is illustrated in Figure 2-2.

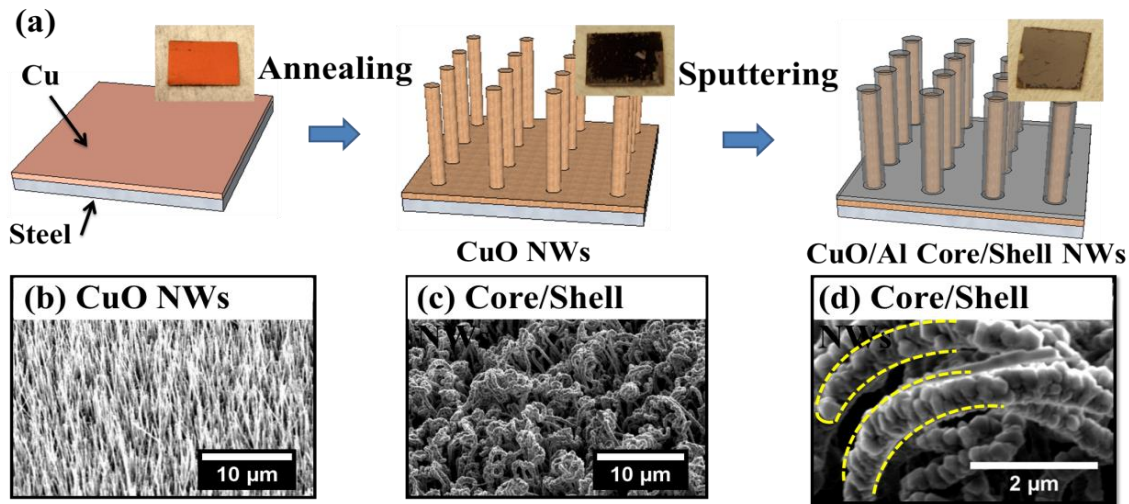


Figure 2-2: a) Schematics of the fabrication process of the CuO/Al core/shell NWs. The insets are the corresponding optical images. SEM images of the b) CuO NWs, c) CuO/Al (250 nm) core/shell NWs, and d) enlarged view of c). The yellow dashed lines outline each core/shell nanowire.

First, a layer of copper film was electroplated over a steel plate using a flash copperTM plating kit (Castwell Inc.) with a current density of 20 mA/cm², which yields a deposition rate of approximately 60 nm/min.¹ We deposited a copper film of 1 μm thickness because it gives the optimum CuO NW density with a thin supporting CuO layer. Before electroplating, the steel plate was thoroughly cleaned with acetone, methanol, and isopropyl alcohol, in sequence, to remove any organic impurities and promote the adhesion of copper. Second, CuO NWs were grown by the simple thermal annealing method, [57] in which the electroplated copper film was heated on a hotplate at 500 °C for 5 or 24 hours under ambient conditions. After annealing, the color of the copper film changed from shiny brown to black (Figure 2-2a, inset), indicating that Cu has been oxidized to CuO. Scanning electron microscopy (SEM, FEI XL30 Sirion, 5kV) imaging (Figure 2-2b) shows that CuO NWs have been formed with a perpendicular orientation with respect to the Cu film. Finally, a layer of Al film was deposited over the CuO NWs by magnetron sputtering under a vacuum level of 5×10^{-3} Torr. Magnetron sputtering was selected over other metal deposition techniques, such as electron beam and thermal evaporation, because it provides enhanced conformal coating, resulting in a uniform CuO/Al core/shell NW structure (Figure 2-2c, and d). Since the deposition rate on the sidewall of NWs is typically smaller than that on a flat surface, the actual thickness of the Al layer was always measured by the SEM. The Al layer thicknesses analyzed in this paper were set to be 0.5, 1.0, 1.5 μm for a flat surface, and the actual shell thicknesses are around 100, 250, and 425 nm. The morphology and surface coverage density of the CuO NWs can be easily tuned by varying the annealing temperature and time. For example, the CuO NWs grown for 5- and 24-hour annealing

were compared in **Error! Reference source not found.** The average length and diameter of the CuO NWs are 3 - 7 μm and 40 - 90 nm for the 5-hour annealing case and 12 - 16 μm and 50 - 100 nm for the 24-hour annealing case, respectively. The surface density of NWs for the 24-hour annealing case, estimated on the basis of SEM images (**Error! Reference source not found.b**), is about 10^8 - 10^9 NWs/ cm^2 , which is significantly larger than that of the 5-hour annealing case (**Error! Reference source not found.a**).

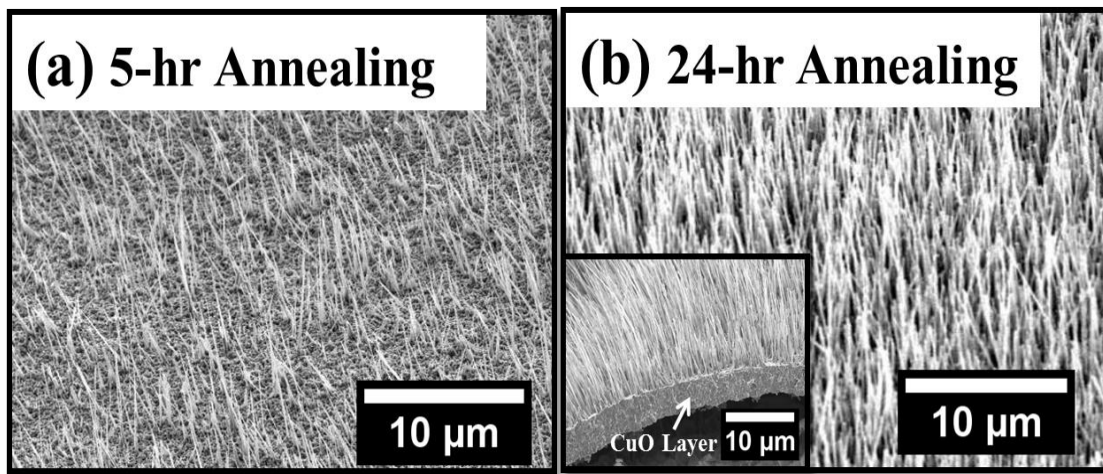


Figure 2-3: Effect of the growth time on the morphology of the CuO NWs annealed at 500 °C. SEM images of NWs grown for a) 5 hours and b) 24 hours. The inset shows that the CuO NWs are connected to the underneath CuO layer.

As such, the annealing conditions provide a convenient way to control the amount of CuO loading per unit area for the thermite reaction. All the results reported here were based on the CuO NWs synthesized for 24 hours. It should be noted that a

CuO layer of approximately 3 μm thickness is formed immediately beneath the CuO NWs during the growth process (**Error! Reference source not found.**b, inset) which, together with the CuO NWs, easily separates from the underlying steel plate. The CuO layer cannot be isolated from the CuO NWs, so it is also a part of the thermite sample. The exact equivalence ratio of the CuO/Al thermite cannot be calculated accurately because the NWs cannot be cleanly separated from the underlying CuO layer (Fig. 2b inset). Hence, increasing the thickness of the Al layer is a qualitative method to increase the overall fuel/oxidizer equivalence ratio. In addition, we tested commercial CuO NPs and Al NPs in order to compare the differences between NP-based and NW-based thermites. The Al NPs (SkySpring International, Inc.) and the CuO NPs (Inframat Advanced Materials) have average diameters of 80nm and 60nm, and densities of 2.7 g/cm^3 and 6.3 g/cm^3 respectively. The CuO/Al NPs mixtures were prepared in different equivalence ratios by manual mixing.

2.3.2. Synthesis and characterization of Al/CuO core/shell particles

Here, we report an effective method to modify the ignition and combustion properties of Al NPs and MPs by coating them with a thin CuO shell using a solution phase method. This solution phase synthesis is an extension of the core/shell NWs synthesis method, since it can produce large yields of sample mass to enable the burning rate measurement. Moreover, it is of great practical interest to tailor the ignition and combustion properties of Al MPs to be comparable to those of Al NPs because Al MPs are about 30 – 50 times cheaper than Al NPs [58] and contains more Al content per particle.

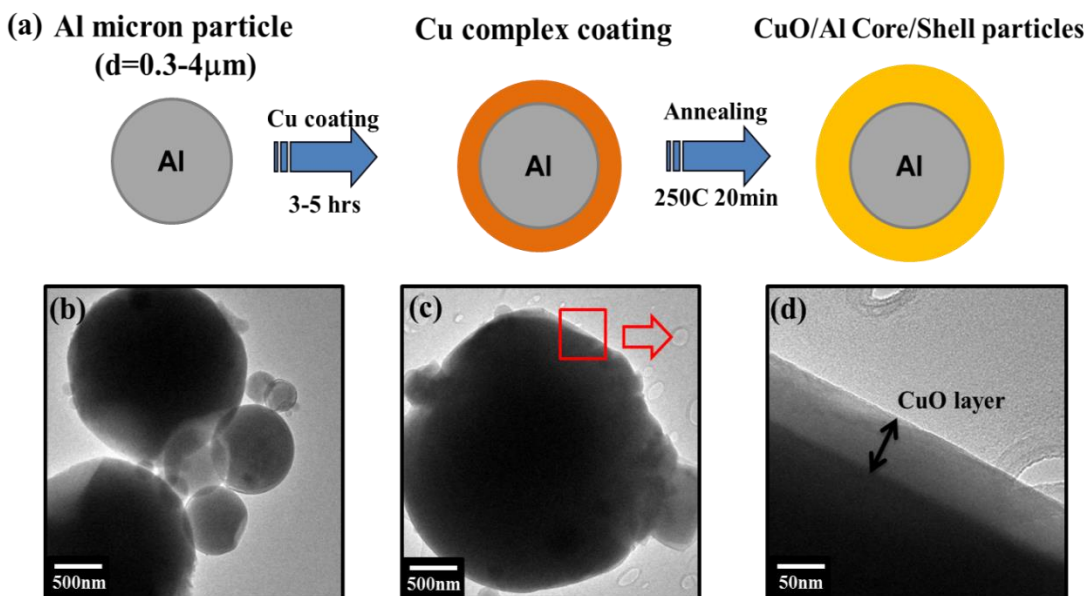


Figure 2-4: a) Schematics of the synthesis process of the Al/CuO core/shell particles. TEM images of the b) initial Al particles, c) Al/CuO core/shell particle, and d) enlarged view of c).

The coating of Al particles with a CuO shell to form Al/CuO core/shell particles was accomplished in two steps: hydrolysis/condensation and annealing, as illustrated in Figure 2-4. First, 0.5 g of either Al NPs ($d_{\text{avg}} = 80 \text{ nm}$, SkySpring International Inc.) or Al MPs ($d_{\text{avg}} = 2.3 \mu\text{m}$, Atlantic Equipment Engineers) were added into 100 ml absolute ethanol (200-proof) and then stirred and sonicated for 10 minutes, resulting in a gray colloidal suspension. Next, 2 ml of aqueous ammonium hydroxide (NH_4OH , 15%) and 1 g copper nitrate ($\text{Cu}(\text{NO}_3)_2 \cdot 2.5\text{H}_2\text{O}$, 99.99%, Sigma-Aldrich) in 10 ml ethanol solution (0.43M) were slowly added together into the colloidal suspension. After the addition, the resulting colloidal suspension was stirred for 3 hours and the color of the suspension changed from gray to blue gray. During this process, Cu^{2+} ions reacted with

ammonia and formed $[\text{Cu}(\text{NH}_3)_4]^{2+}$ ions that electrostatically combined with the OH^- ions on the Al particle surface, forming a condensed shell of copper complex ($\text{Cu}(\text{NH}_3)_4(\text{OH})_2$). [59] The suspended Al/copper complex core/shell particles were collected by vacuum filtration through filter paper (Whatman, grade 42), and the retrieved particles were further passed through a 140-mesh sieve to break up large agglomerates. The collected particles were annealed at 250 °C for 30 minutes on a hotplate under ambient conditions, and the color of the particles changed from blue gray to dark gray, indicating that the copper complex shell was oxidized to CuO. Finally, we obtained the Al/CuO core/shell particles and the CuO shell thickness can be controlled by varying the stirring time to adjust the amount of the copper complex deposited on the surface of Al particles.

Please note that extreme care should be taken during the annealing procedure since the particles can self-ignite when the annealing temperature reaches approximately 300 °C.

In addition to the Al/CuO core/shell particles, we also prepared simple mixtures of Al particles (both NPs and MPs) and CuO NPs ($d_{\text{avg}} = 60$ nm, Inframat Advanced Materials) as reference samples for control experiments. These reference mixtures were prepared by the method reported in Ref. [60]. Mixtures of Al and CuO particles were placed in a glass beaker and sonicated for 15 minutes with 100 ml of hexane. After sonication, the mixtures were collected by paper filtration and passed through a 140

mesh sieve to break up large agglomerates. Finally, the collected powders were dried on a hotplate at 60 °C for 30 minutes to remove the hexane.

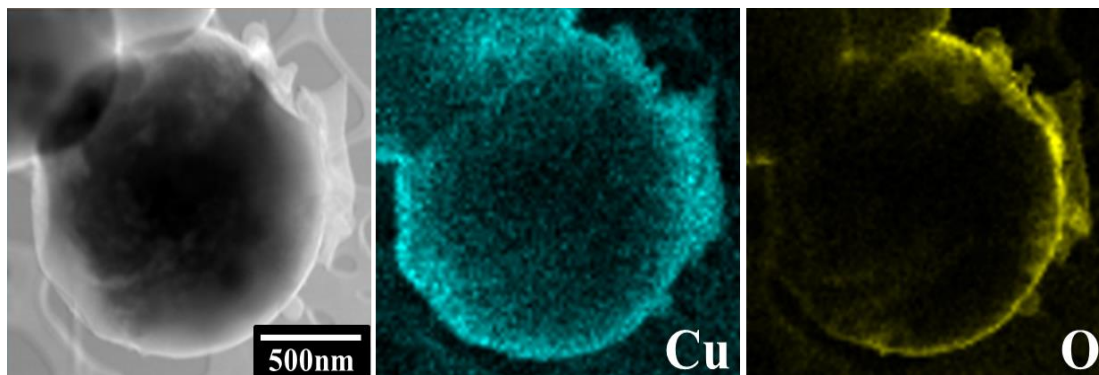


Figure 2-5: a) TEM image of the Al/CuO core/shell MP. b) and c) EDS elemental mapping images of Cu and O.

The morphology of the Al/CuO core/shell particles was characterized by transmission electron microscopy (TEM, FEI Tecnai G2 F20 X-TWIN FEG, 200 kV). The initial Al NPs were spherical and highly agglomerated with an average diameter of 80 nm and a 2 nm thin native aluminum oxide (Al_2O_3) shell. The Al MPs had a broader diameter distribution ranging from 0.3 to 4 μm with a 5 nm thin Al_2O_3 shell. After the copper complex coating and annealing process, the Al particles were coated with a thin CuO shell of approximately 20 - 50 nm thickness for Al MPs (Figure 2-4c and d) and thinner for Al NPs. The chemical compositions of the core/shell particles were analyzed by Energy-Dispersive X-ray Spectroscopy (EDS) element mapping (Figure 2-5b and c), which clearly reveals the presence of Cu and O on the Al particle surface, indicating the formation of the Al/CuO core/shell particle structure.

The mass ratios between Al and Cu for the core/shell particles were measured by Inductively Coupled Plasma Optical Emission Spectroscopy (ICP-OES, Thermo Scientific ICAP 6300 Duo View Spectrometer), and are Al:Cu = 1.8:1 and 2.3:1 for the CuO-coated Al NPs and MPs, respectively. Assuming that all the Cu in the core/shell particles has been oxidized to CuO, the calculated equivalence ratios (Φ) are 6.3 and 8.1 for the CuO-coated Al NPs and MPs, respectively. Both Al/CuO core/shell NPs and MPs were rich in Al and the NPs contain slightly more CuO than the MPs due to the larger surface to volume area.

2.4. Synthesis of freestanding porous Si film

The freestanding porous Si film is prepared by electrochemically etching Si wafers (p-type, 0.1 – 0.9 $\Omega\cdot\text{cm}$), followed by an electropolishing step to release the porous Si film from the Si wafer. Specifically, a 200 nm-thick Al film is first deposited on the back of Si wafers, followed by half an hour annealing at 400°C to form an electrical contact to serve as an electrode for the following electrochemical etching step. The Si wafer containing the Al back contact is then placed in a Teflon anodization cell (Error! Reference source not found.) filled with an ethanolic HF electrolyte solution mixture of 48% HF and 100% ethanol). The concentration of the solution is varied among three volumetric ratios (HF:ethanol = 1:0.5, 1:0.75, 1:1) to alter the porosity of the final porous Si film. A constant current of 50 mA/cm² is applied between the Al electrode on the back of the Si wafer and a Pt counter electrode submerged in the

ethanolic HF solution for 2 - 40 minutes to control the porous Si film thickness (**Error! reference source not found.**). [61, 62]

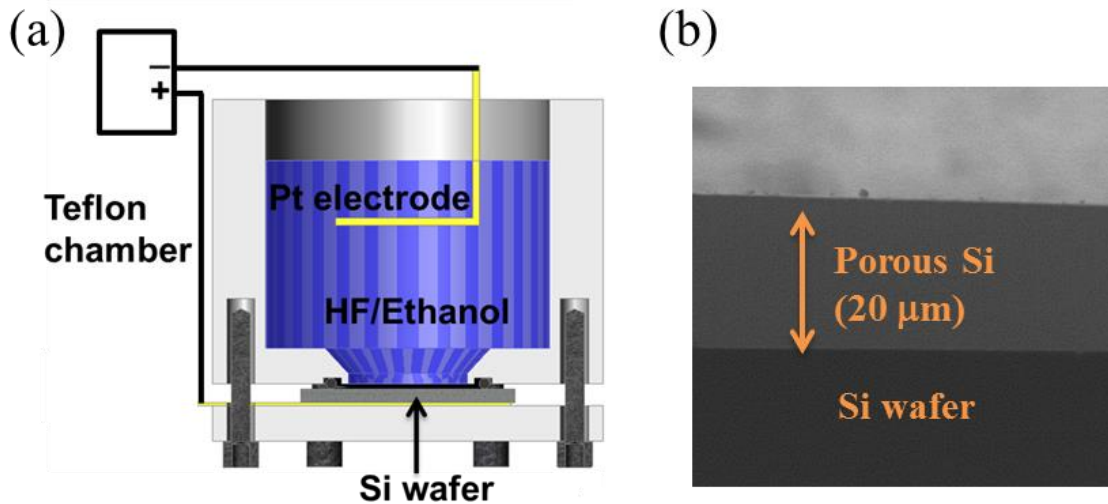


Figure 2-6: (a) Cross-sectional schematic of an anodization cell used for the porous Si formation, and electropolishing. [63] (b) Cross-sectional SEM image of the porous Si layer formed over the Si wafer.

Next, the etched porous Si film is detached from the Si wafer by increasing the current to 200 mA/cm^2 for 15 sec due to electropolishing. [62-66] Finally, the detached porous Si film is removed from the anodization cell and dried with a critical point dryer (Samdri-PVT-3B, tousimis) to prevent porous Si films from cracking.

2.5. Conclusion

We have demonstrated the synthesis of core/shell structured energetic materials, and freestanding porous Si film. The synthesis of the NW thermites involved two simple steps: 1) growing CuO NWs by the thermal annealing of copper and 2) depositing a layer of Al by magnetron sputtering. The synthesis of core/shell particles was achieved by coating the Al particles with a very thin CuO shell using a simple solution phase method. The solution phase method can produce large yields of sample mass to enable combustion characterization measurement. Both core/shell NW-based and particles-based Al/CuO composite have excellent chemical homogeneity. The synthesis of freestanding porous Si film involved electrochemical etching to form the porous Si layer and electropolishing to release the porous Si film from the Si wafer. The etching time and HF concentration of the solution were varied to control the film thickness and porosity. We believe that the core/shell and porous structure synthesis methods can be applied to other metal, metal oxide, and semiconductor material thereby opening up more opportunities as an ideal energetic structure for tuning their ignition and combustion properties.

3. Enhanced exothermic reaction of core/shell structured materials

Chapter 2 has discussed the synthesis of energetic CuO/Al core/shell NWs and Al/CuO core/shell particles. Both core/shell NW-based and particles-based Al/CuO composite were synthesized to demonstrate the excellent chemical homogeneity. In this Chapter, we analyze the enhanced exothermic reaction behavior of the synthesized core/shell structured energetic materials.

3.1. Experimental specifications

3.1.1. Differential scanning calorimetry

Differential scanning calorimetry (DSC) is a standard technique in solid-state chemistry to understand the solid interactions while precisely heating up the sample to the programmed condition. The role of a DSC device is to measure the heat flow rate as a function of temperature. The measurement results can be used to trace the exothermic/endothermic oxidation/reduction reactions, phase changes and determine reaction kinetics of various materials. Inside the DSC furnace the sample and reference are both maintained at the programmed temperature during a thermal event. When a change in temperature is detected between the sample and the reference, the input power to the sample is controlled to equilibrate the temperature. This allows to

quantitatively determine the change in the heat flow rate of the sample during a reaction. The onset temperature and heat release characteristics of the energetic core/shell structured materials were studied using differential scanning calorimetry (DSC, SETSYS Evolution DTA/DSC). Before each test, the DSC chamber was evacuated and flushed twice with inert He gas to remove any residual air. The sample was then heated from room temperature in the DSC furnace under the inert He environment with a controlled heating rate of 5 °C/min between 350 °C and 800 °C, unless otherwise specified. The CuO/Al core/shell NWs, approximately 10 mg, were scraped from the steel plate with a razor and placed in an inert alumina crucible during the DSC measurement. Similarly, for the core/shell particles, 10 mg of the sample powders were placed in the alumina crucible. The heat release was calibrated against a standard KBr sample with a known heat of fusion of 216 ± 3 J/g at a melting temperature of 1007 K [67] shown in Figure 3-1. The heat release traces reported here were baseline-corrected after collecting the data.

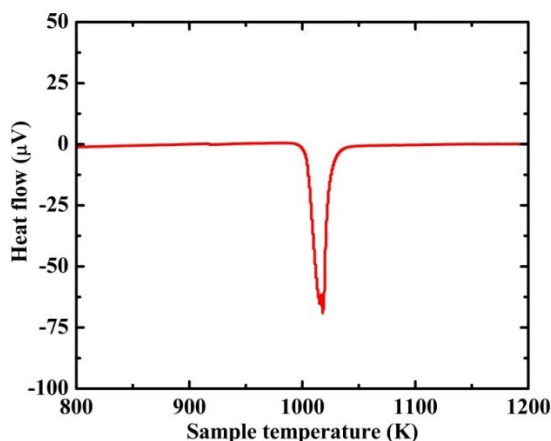


Figure 3-1: The DSC calibration curve measuring the heat of fusion of KBr (56.85 mg). The integrated area under the heat of fusion curve is 51.956 $\mu\text{Vs/g}$.

3.1.2. X-ray diffraction analysis

The X-ray power diffraction analysis provides information of crystalline phases, individual crystal size and elements the energetic materials. The compositions of the CuO/Al core/shell NW samples were analyzed by parallel beam X-ray diffraction (XRD, PANalytical XPert 2, Cu $K\alpha$, 45 kV, 40 mA) before and after the DSC measurement. The typical XRD spectra of the initial reactants and final products are shown in Figure 3-2. The XRD spectrum of the initial CuO/Al core/shell NWs, as expected, shows two major crystalline phases, corresponding to CuO and Al, respectively. After heating the sample up to 800 °C in the DSC, the XRD spectrum of the final product exhibits dominant peaks of Cu₂O and smaller peaks of CuO and Al, indicating that CuO has been reduced by Al. The absence of Al₂O₃ peaks is probably due to the fact that the Al₂O₃ product phase is amorphous or poorly crystalline. [68]

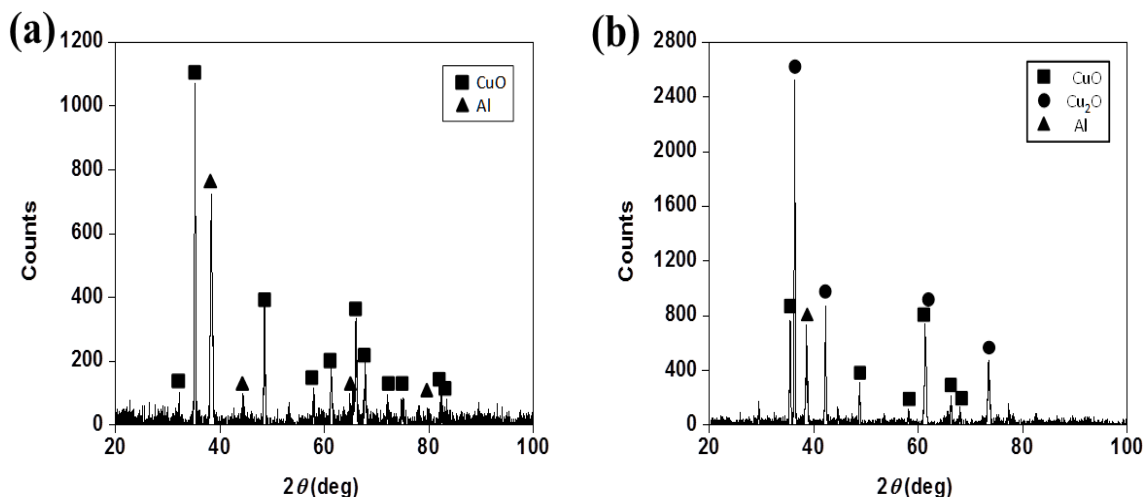


Figure 3-2: Parallel beam XRD of CuO/Al (250nm) core/shell NWs a) before and b) after the DSC test.

3.1.3. Burning rate measurement

The core/shell structure improves the chemical homogeneity of Al and CuO, which is expected to increase the burning rates. Such effects were studied by measuring the burning rate of the Al/CuO core/shell particles and reference samples (simple mixtures of Al and CuO particles) in an unconfined microchannel (Figure 3-3) that was integrated with a fiber-optic probe platform. [69]

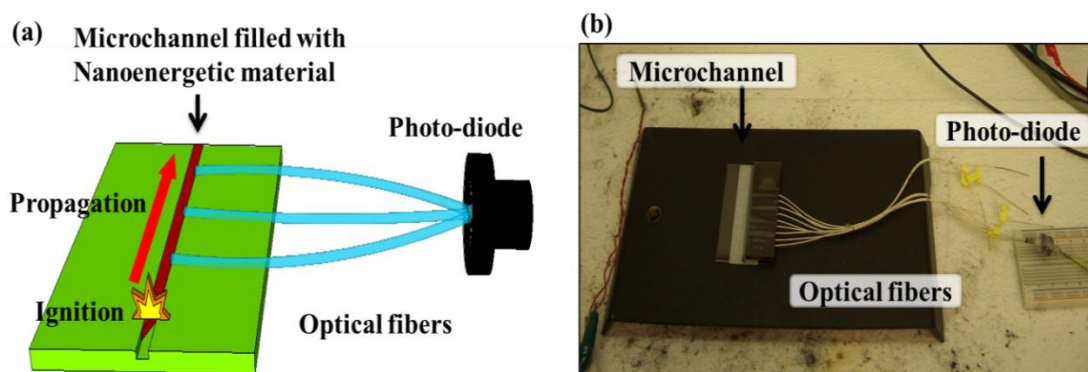


Figure 3-3: a) Schematic and b) optical image of the microchannel device for burning rate measurement. The thermite reaction propagates across the microchannel associated with the visible emission, which was collected by the photo-diode through an equally-spaced array of optical fibers.

Specifically, the microchannel was made of glass and had a depth of 1 mm and a width of 500 μm for measurement of the Al/CuO core/shell NPs and a width of 830 μm for measurement of the core/shell MPs. The channel width was increased to 830 μm for

the core/shell MPs because their reaction was quenched at 500 μm . Five fiber-optic probes were placed at 10 mm intervals along the microchannel and connected to a photo-diode. These fiber-optic probes captured the optical emission from the thermite reaction front and the photo-diode further converted the optical signals into voltage signals that were read out by an oscilloscope. The flame propagation speed was determined by dividing the distances between the five fiber-optic probes by the time delay between the voltage peaks. The advantage of the microchannel is that smaller quantities of energetic materials ($< 5\text{ mg}$) can be used, than are required in larger scale tests (a few hundred mg), [60] which improves safety during the measurement. Nevertheless, the microchannel is associated with a greater amount of heat loss due to the increased surface-to-volume ratio. Thus, the measured flame propagation speeds are useful for quantitative comparison between samples measured in the same configuration, and cannot be used for quantitative comparison to burning rates measured in other experimental configurations, due to the differences in the experimental setup, such as confined/unconfined channel, dimensions and materials of the channel, and the larger heat loss associated with microchannels. [70]

3.2. Exothermic reaction of CuO/Al core/shell nanowires

3.2.1. Effect of the Al layer thickness

Figure 3-4 shows the effect of the Al layer thickness on the exothermic heat release of the CuO/Al core/shell NWs.

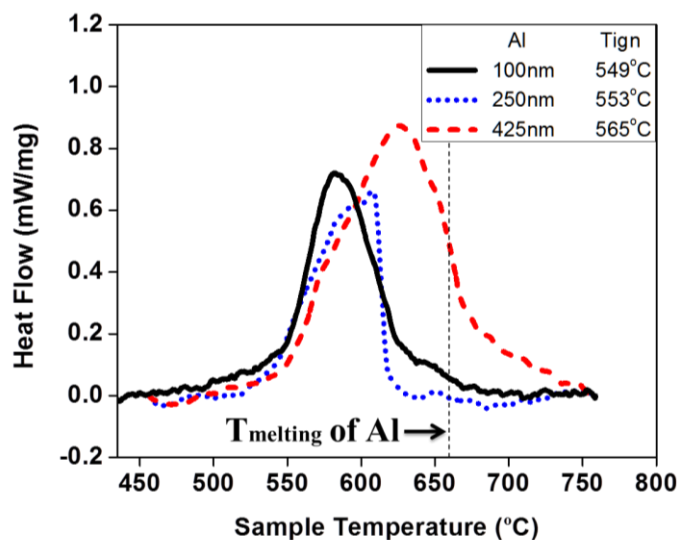


Figure 3-4: DSC traces for reactions of the CuO/Al core/shell NWs with different Al shell thickness (100 nm, 250 nm, and 425 nm). All the traces were recorded in inert He at a heating rate of 5 °C/min.

The average thicknesses of the Al layer of the three tested samples are 100, 250, and 425 nm respectively. The exact equivalence ratio of the CuO/Al thermite cannot be estimated accurately because the NWs cannot be separated from the underlying CuO layer without damaging the NWs. Hence, increasing the thickness of the Al layer is a qualitative method to increase the overall fuel/oxidizer equivalence ratio. First of all, the onset temperature of the exothermic thermite reaction is around 560 °C for all three cases. The exothermic onset temperature of the CuO/Al NWs is below the melting temperature of Al (660 °C) and much lower than the exothermic onset temperature (1040 °C) of micron-sized stoichiometric CuO and Al mixture under the same test conditions. This supports the fact that reducing the dimensions of CuO and Al to the nanoscale can significantly facilitate the ignition process. [71] Second, the exothermic

onset temperature of the CuO/Al NWs only increases by about 16 °C when the Al layer thickness is increased by more than four times (Figure 3-4). The insensitivity of ignition temperature to the equivalence ratio was also observed previously for the laser ignition of Al/MoO₃ nano-thermites prepared by ultrasonic mixing of respective NPs, for which the ignition delays show little variation over the equivalence ratio range of 0.5 – 2. [72] Finally, there was no endothermic peak observed at the melting temperature of Al for any of the three CuO/Al core/shell NWs, suggesting that there is no Al left unreacted. The endothermic peak has been observed for both CuO/Al NPs and similar CuO/Al core/shell NWs, for which Al was deposited by thermal evaporation. [51] It indicates that our fabrication method, combining long growth time of CuO NWs and conformal coating of Al with magnetron sputtering, generates spatially-uniform CuO/Al nano-thermite without local accumulation of Al, as observed in the case of mixing NPs.

3.2.2. Effect of heating rate

The ignition and heat release characteristics of the CuO/Al core/shell NWs with 250 nm thick Al layers were further studied and compared under different heating rates. The effect of heating rate is not only of practical importance because different ignition methods have different heating rates, but also of fundamental interest because the heating rate can affect the reaction mechanism of nano-thermites. [71]

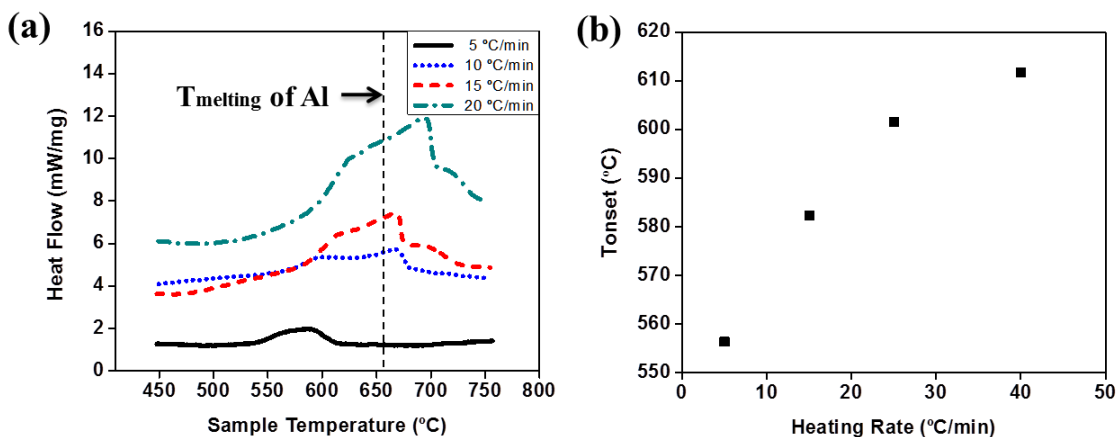


Figure 3-5: a) DSC traces for reactions of the CuO/Al (250nm) core/shell NWs at heating rates of 5 °C/min, 15 °C/min, 25 °C/min and 40 °C/min. b) The exothermic onset temperatures of the CuO/Al core/shell NWs at different heating rates.

First, as shown in Figure 3-5a, the heat release profile broadens as the heating rate is increased. This is due to the fact that, under larger heating rates, the sample experiences larger spatial heterogeneity in terms of temperature and the onset of reaction, so the heat release profile tends to be broader. Second, no endothermic peak associated with the melting of Al was observed in all the cases with different heating rates, which again supports the fact that Al was coated over the CuO NWs with excellent spatial uniformity without local accumulation. Finally, the exothermic onset temperature of the CuO/Al NWs increases significantly with increasing heating rate, as shown in Figure 3-5b, a typical characteristic of the thermal lag due to the larger heating rate. For instance, the exothermic onset temperature is increased by more than 50 °C when the heating rate is increased from 5 °C/min to 40 °C/min, and is far more sensitive to the heating rate than to the equivalence ratio (Figure 3-4). Such a strong dependence

of the exothermic onset temperature on the heating rate is similar to that of Al/MoO₃ NP thermites reported by Pantoya and Granier. [71]

The global activation energy of the CuO/Al core/shell NW thermite reaction was extracted on the basis of the Kissinger relation [73, 74]:

$$\frac{T_p^2}{\beta} = A \exp\left(\frac{E_a}{RT_p}\right) \quad (1)$$

, where T_p (K) denotes the temperature at which the peak heat release occurs, β the heating rate (°C/sec), E_a the activation energy (kJ/mol), R the universal gas constant and A a constant. Therefore, the activation energy E_a can be calculated from the slope of the $\ln(T_p^2/\beta)$ vs. $1/T_p$ curve, as shown in Figure 3-6.

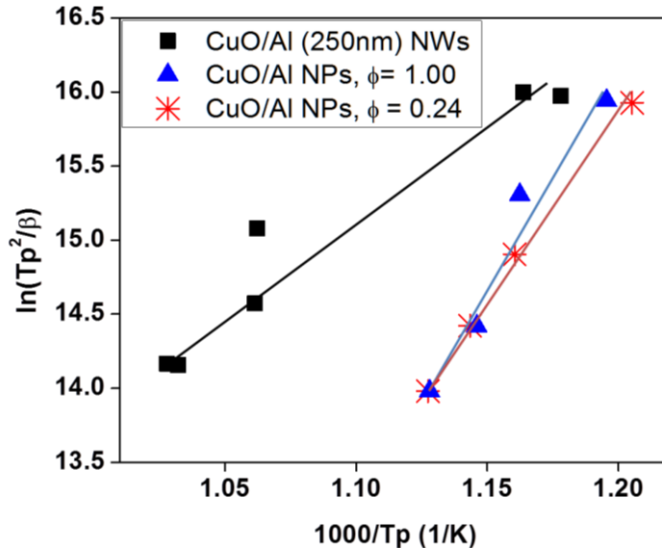


Figure 3-6: Thermal analysis of DSC traces for the CuO/Al (250 nm) core/shell NWs, and CuO/Al NPs at equivalence ratios of 1.00 and 0.24.

The extracted E_a for the CuO/Al core/shell NWs with 250 nm thick of Al layer is about 102 kJ/mol. We also performed the DSC measurements of the mixture of CuO NPs and Al NPs under different heating rates as a comparison. The activation energies E_a of the CuO/Al NP thermites are about 250 and 207 kJ/mol for the equivalence ratio of 0.24 and 1.00 respectively. Although the exact equivalence ratio of the CuO/Al core/shell NWs is unknown, its E_a is almost half of both the fuel-lean and stoichiometric CuO/Al NPs, suggesting that the thermite reaction between CuO and Al in this core/shell NW structure occurs more readily than that in the NP mixtures. One potential reason is that the native Al_2O_3 shell outside the Al NPs has to be melted or broken in order for Al to contact CuO for reaction. However, Al is already in contact with CuO in the core/shell NW structure. Even though there may exist a partially reacted interface between CuO and Al after the deposition of Al, this layer, unlike the outermost Al_2O_3 shell, does not require to be melted or broken for reaction to initiate. Consequently, oxygen only needs to diffuse within the NWs which facilitates the reaction of the core-shell NWs.

3.2.3. Comparison of nanowire- and nanoparticle-based thermites

To further explore the potential of NW-based thermites, we have compared the heat release behaviors of three samples, *i.e.*, the CuO/Al core/shell NWs (Al thickness: 425 nm), a stoichiometric mixture of CuO NWs and Al NPs (80 nm), and a stoichiometric mixture of CuO NPs (60 nm) and Al NPs (80 nm). All three samples

were heated under inert He environments inside the DSC furnace with a heating rate of 5 °C /min, and their typical DSC traces are shown in Figure 3-7.

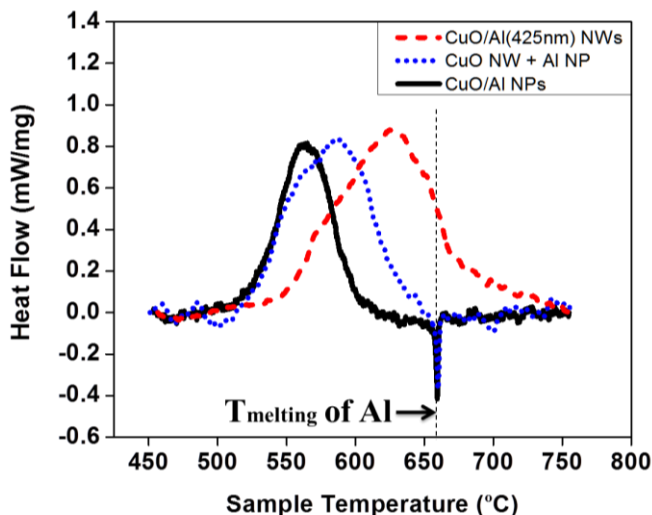


Figure 3-7: Comparison of DSC traces for reactions of CuO/Al (425nm) core/shell NWs, a stoichiometric mixture of CuO NWs and Al NPs, and a stoichiometric mixture of CuO and Al NPs.

First of all, although the heat release profiles of all three samples have well-defined single peaks, the widths of the heat release profiles are much broader for the two samples containing CuO NWs. One possible reason is that the CuO NWs scraped from the steel plate always contain some of the CuO thin film layer, which reacts with Al at higher temperature compared to the CuO NWs, leading to the broadening of the heat release profile. In other words, the overall reaction proceeds in two steps: CuO NWs first react with Al followed by the reaction between the CuO layer and Al. Second, all three samples have very similar exothermic onset temperatures, 550 °C for the

CuO/Al core/shell NWs, 545 °C for the CuO NWs/Al NPs and 540 °C for the CuO NPs/Al NPs, which are below the melting temperature of Al. This suggests that ignition of nano-thermites, regardless of their morphologies and structures, is greatly facilitated by reducing the diffusion length of oxygen. In addition, the CuO film layer seems to have a negligible effect on the exothermic onset temperature, suggesting that ignition is initiated by reaction between the CuO NWs and Al.

More importantly, one distinctive feature of the heat release profile for the CuO/Al core/shell NW sample (Figure 3-7) is the lack of the endothermic peak around the melting temperature of Al (660 °C). However, such an endothermic peak, for both the CuO NWs/Al NPs and the CuO NPs/Al NPs samples, appears after the heat flow has leveled off, indicating there are some Al NPs left after the thermite reaction, although both samples are stoichiometric and, in theory, Al should have been totally consumed. Moreover, such endothermic peaks were also observed for fuel-lean CuO NPs/Al NPs samples of equivalence ratio of 0.50 and 0.24 and stoichiometric CuO/Al nanocomposites samples prepared by arrested reactive milling reported by Umbrajkar et al. [68] It suggests that it is difficult or even impossible to achieve perfect spatial uniformity by mechanically mixing two solid phase components. In other words, there will always be regions of more Al and regions of less Al, so that some Al will be left unreacted. On the contrary, in the case of CuO/Al core/shell NWs, the CuO NWs provide an excellent template for the uniform coating and distribution of Al. Even though the core/shell NWs can be broken into pieces during the sample handling process, each piece is still a uniform CuO/Al mixture so that there is no pocket of Al

accumulation and the corresponding endothermic peak. Hence, the current CuO/Al core/shell NW structure significantly improves the overall spatial uniformity of the nano-thermites, and provides an ideal platform for the study of the thermodynamic and kinetic properties of nano-thermites. Finally, the similarities observed for the CuO NWs/Al NPs and the CuO NPs/Al NPs samples suggest that synthesis of CuO NWs by thermal annealing is a simple and convenient way to produce nanostructured CuO for thermite reactions.

3.3. Enhanced combustion of Al/CuO core/shell particles

From the discussion above, the excellent spatial uniformity of the core/shell NW structure has shown promising reaction characteristics in the DSC measurements. While maintaining the core/shell structure, we next characterize of the Al/CuO core/shell particles. The Al/CuO core/shell particles, unlike core/shell NWs can be synthesized via solution phase method that could produce large yield of sample mass to enable the burning rate measurement. To investigate and understand the effects of the core/shell structure on burning rate, we conducted DSC, and burning rate measurements, for both the Al/CuO core/shell particles (both NPs and MPs) and reference mixtures of Al particles and CuO NPs. The reason for using CuO NPs for the reference mixtures is to simulate the nanoscale thickness of the CuO shell in the core/shell particles, without the intimate contact of Al and CuO.

3.3.1. Effect of structure on the onset temperature

The onset temperatures of the Al/CuO core/shell particles and mixture of Al particles and CuO NPs were measured by DSC. As shown in Figure 3-8, the onset temperature for the exothermic reaction of $\text{Al} + 3\text{CuO} \rightarrow 1/2\text{Al}_2\text{O}_3 + 3/2\text{Cu}_2\text{O}$ is around 520 °C for each of the four samples: 532 °C for the Al/CuO core/shell NPs, 516 °C for the NP mixture ($\Phi = 6.3$), 510 °C for the Al/CuO core/shell MPs, and 536 °C for the MP mixture ($\Phi = 8.1$). The endothermic peaks at 660 °C are due to the melting of Al. The similar onset temperatures between the Al/CuO core/shell MPs and the mixture of Al MPs and CuO NPs suggest that the increase in contact area between the Al and CuO has a slight effect on the onset temperature of Al/CuO exothermic reaction. On the other hand, the smaller endothermic peak of the core/shell particle structure indicates the lesser amount of unreacted Al left after the thermite reaction, which agrees with the DSC analysis results from the core/shell NWs structure.

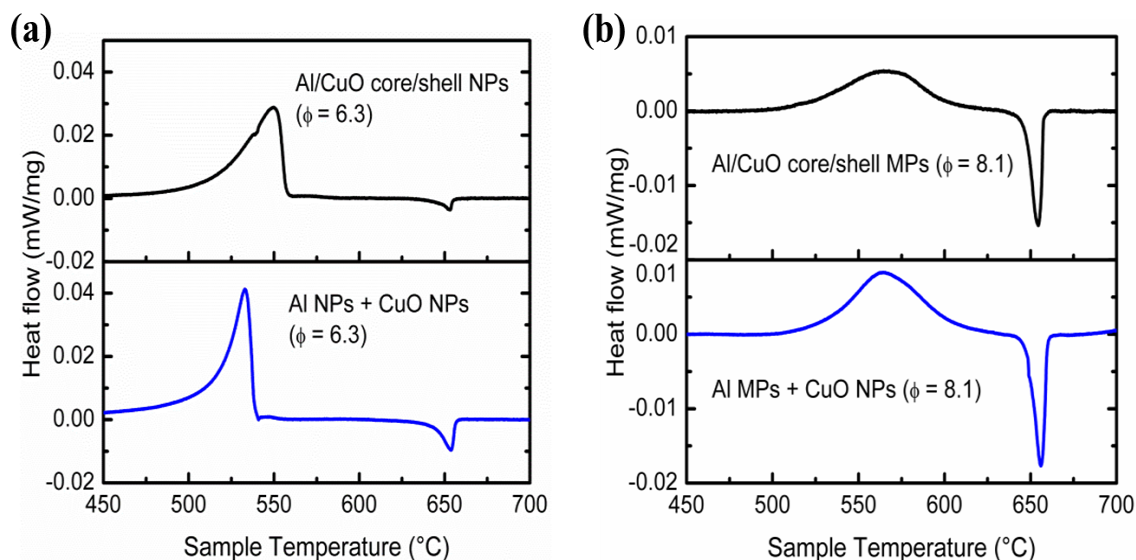


Figure 3-8: Comparison of DSC traces for reactions of Al/CuO core/shell (a) NPs and (b) MPs vs. mixtures of Al NPs and CuO NPs with same equivalence ratio ($\Phi = 6.3$, 8.1).

3.3.2. Effect of the core/shell structure on the burning rates

Next, we further investigated the effect of core/shell structure on reaction rates by comparing the burning rates of the Al/CuO core/shell particles and their reference mixtures with the same equivalence ratios. First, as shown in Figure 3-9 for the NP samples, the Al/CuO core/shell NPs have about 25 times larger burning rate than that of the mixture of Al NPs and CuO NPs. Second, the Al/CuO core/shell MPs even with such extremely high Φ of 8.1, were able to propagate along the microchannel and exhibited smaller quenching channel width than that of the reference mixture of Al MPs and CuO NPs with the same Φ . Both comparisons illustrate that the core/shell particle structure has the advantages of better chemical homogeneity and physical contact

between Al and CuO, leading to higher reaction rates and larger burning rates than those of the mechanically mixed samples.

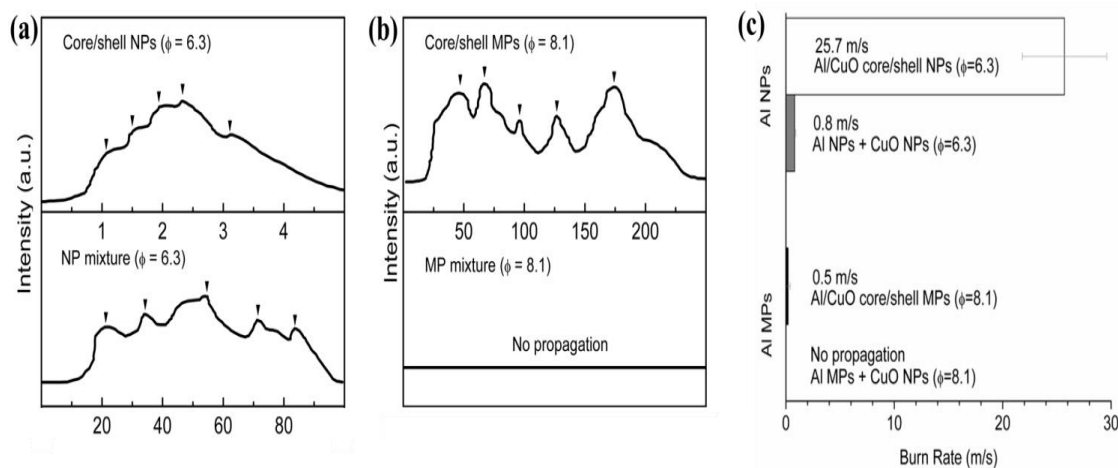


Figure 3-9: Photo-diode signal voltages as a function of time for Al/CuO core/shell (a) NPs and (b) MPs compared to Al/CuO powder mixtures at equivalent stoichiometry. The peak signal voltages are indicated by the reverse triangle and the burn rate is determined by dividing the distances between the five fiber-optic probes by the time delay of the peak voltages. (c) Comparison of burn rates of Al/CuO core/shell particles vs. mixture of Al particles (both NPs and MPs) and CuO NPs

3.4. Conclusion

In summary, we have experimentally determined the exothermic onset temperatures and heat release characteristics of energetic CuO/Al core/shell structures for both NWs and particles through DSC measurements. The exothermic onset

temperature of the core/shell NWs is about 100 °C below the melting temperature of Al and insensitive to the CuO/Al equivalence ratio. The CuO/Al core/shell NWs, comparing to conventional nano-thermites prepared by mixing NPs, has no endothermic peak associated with residual Al melting in the heat release profile and has significantly reduced activation energy for the thermite reaction between CuO and Al. Similarly, for core/shell particles, the increase in the contact area between Al and CuO has a small effect on onset temperatures compared to that of mixtures of Al and CuO powders. The smaller endothermic peak of Al melting compared to the powder mixture was also observed for the core/shell particle structure suggesting that the increase in the contact area enhances the fuel utilization of Al. Finally, the Al/CuO core/shell particles exhibit burning rates larger than those of the mixture of Al and CuO powders. These observations suggest the great potential of core/shell structure thermites due to their excellent spatial uniformity, large reactivity and applicability to other material compounds.

4. Flash ignition of Al particles and addition of WO₃ nanoparticles

4.1. Background

Aluminum is an important fuel for various propulsion systems due to its large energy density (83.8 kJ/cm³), [18] twice as high as that of gasoline (34.2 kJ/cm³). For micron-sized Al particles, their combustion process is similar to that of liquid droplet combustion (d^2 law) [75] and the oxidation process occurs after the melting of the outer aluminum oxide. On the other hand, Al NPs, comparing to micron-sized Al particles, have a much lower ignition temperature (~ 900 K), [76, 77] faster burning rates (~ 2400 m/s) [78] and have the potential to improve the performance of various propulsion systems. However, in the field of energetic materials, it remains a challenge to develop a reliable ignition method for practical utilization of the fuel and achieving distributed ignition at multiple locations, thereby can increase reliability of ignition. Especially for Microelectromechanical systems (MEMS) applications, the small fuel quantity and feature size impose a challenge for reliable ignition with common ignition methods requiring physical contact, such as hotwires, heaters, and piezoelectric igniters. [79] Optical ignition by flash, instead, is very attractive because it works without physical contact and can easily achieve distributed ignition at multiple locations, thereby increasing reliability of ignition and flexibility of design. Herein, we applied a flash ignition method [80-84] to Al NPs to study their oxidization behavior at high heating rates. We have further extended the flash ignition to large particle size of Al MPs.

Compared to Al NPs, it is difficult to ignite Al MPs by flash due to their low light absorption and high ignition temperature, and ignition is only possible with a large flash energy ($> 1 \text{ J/cm}^2$ from a xenon flash lamp). [85] From a practical point of view, Al MPs are more suitable for engineering systems since they are 30 – 50 times cheaper, safer to handle, and contain much higher Al content due to the much smaller fraction of dead volume and weight of the inert Al_2O_3 shell. [58] Previous work on the combustion of Al MPs has shown that Al MPs burn much faster with the addition of nanoscale metal oxides. [27] Therefore, we extended the flash ignition to Al MPs by adding WO_3 NPs. We observe that the minimum flash ignition energy (E_{min}) of Al MPs is greatly reduced by adding WO_3 NPs, and investigate the effect of WO_3 NPs addition.

4.2. Experimental specifications

4.2.1. Flash ignition experimental setup

Flash ignition of Al NPs and Al MPs are achieved by using a commercial camera flash (Vivitar 285HV and AlienBees™ B1600 Flash Unit), which is equipped with a xenon lamp. A schematic of the flash ignition experimental setup is shown in Figure 4-3a. Specifically, tens of milligrams of Al powder were placed on top of a 1 mm thick glass slide that was placed directly above the xenon lamp in the air. For each flash ignition experiment, the powders are gently packed into a cylindrical shape (diameter: 6.8 mm, height: 2.6 mm) to maintain the same volume and cross-section area exposed to the flash (Figure 4-3b). To measure the E_{min} , the power setting of the flash is increased until flash ignition occurs. The areal pulse energy of the xenon flash at each

power setting is measured using an optical power detector (XLP12-3S-H2, Gentec-EO USA, Inc) and the xenon flash spectrum is provided from the vendor.

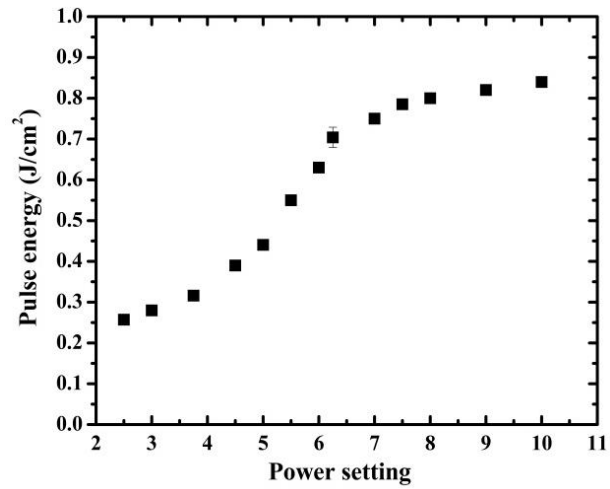


Figure 4-1: Pulse energy calibration with respect to the power setting of the xenon flash

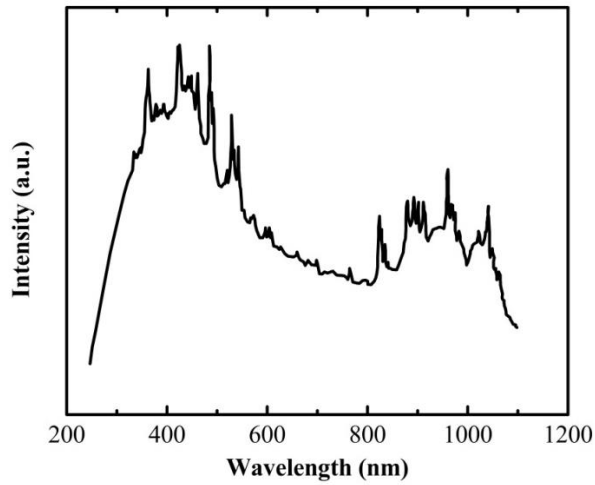


Figure 4-2: Intensity of xenon flash spectrum with respect to wavelength

Flash ignition experiments are carried out in the air, Ar and N₂ atmospheres. For the flash ignition experiments in Ar and N₂, the entire flash unit and samples are placed inside an inflatable polyethylene glove box (Atmosbag glove bag, Sigma-Aldrich) that is purged constantly with pure Ar and N₂.

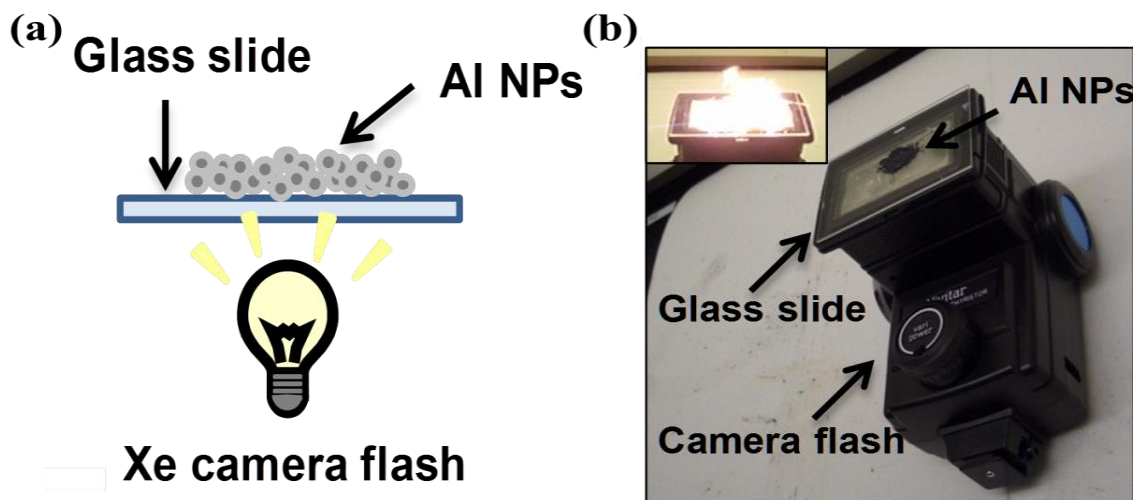


Figure 4-3: (a) Schematic and (b) optical images of the experimental setup for ignition of Al NPs (80 nm) by a camera flash. Inset: photograph of the burning of flash ignited Al NPs which casts a yellow glow and lasts for about 10 s.

4.2.2. Material preparation of Al nanoparticles and mixtures of Al microparticles/WO₃ nanoparticles

We prepared 80 nm Al NPs (SkySpring International Inc.) and two different sizes of Al MPs, *i.e.*, 2.3 μm (Atlantic Equipment Engineers) and 0.9 μm (Sigma-Aldrich). Although the Al NPs are ignited by a single exposure of a xenon flash, flash ignition of 2.3 μm Al MPs was not observed under the maximum flash energy of under 0.84 J/cm² per flash. To extend the flash ignition from nano to micron scale particles,

WO₃ NPs were added to both 0.9 μm and 2.3 μm Al MPs. Mixtures of Al MPs and WO₃ NPs are prepared by ultra-sonication using dimethylformamide (DMF) as a solvent. To study the efficacy of WO₃ NP-assisted flash ignition on Al MPs of different sizes, are separately mixed with WO₃ NPs. Al MPs and WO₃ NPs (80 nm, SkySpring Nanomaterials, Inc) are each weighed to satisfy the targeted fuel/oxidizer equivalence ratio while keeping a total mass of 0.530 g. The Al MP and WO₃ NP mixture is added to 10 ml of DMF and sonicated for 15 mins to ensure uniform mixing. After sonication, the mixture is gently dried on a hotplate at 100 °C for 6 hours to remove the DMF. Finally, the dried mixture powder is passed through a 140 mesh (105 μm) sieve to break up large agglomerates. The Al-to-WO₃ equivalence ratio (ϕ) and normalized equivalence ratio (ϕ_n) of the mixture are defined in Equation (2),

$$\phi = \frac{\left(\frac{m_{Al}}{m_{WO_3}} \right)}{\left(\frac{m_{Al}}{m_{WO_3}} \right)_{st}}, \quad \phi_n = \frac{\phi}{1 + \phi} \quad (2)$$

, where m_{Al} and m_{WO_3} refer to the mass of Al and WO₃, and the subscript *st* refers to the stoichiometric condition for the reaction $2Al + WO_3 \rightarrow Al_2O_3 + W$. Although the Al MPs are encapsulated by a native inert Al₂O₃ shell (2 - 5nm), the active Al content is 97.5 % for the small (0.9 μm) and 99.0 % for large (2.3 μm) Al MPs with a 5 nm shell. Hence, we assume that the entire mass of the Al MPs is Al when calculating the equivalence ratios.

4.3. Flash ignition of Al particles

The Al NPs ignited by a single exposure of a xenon flash (Figure 4-3b) burn in air for about 10 seconds with a yellow glow (Figure 4-3b, inset). The Al NPs change from dark gray, loose powders to light gray aggregated particles after combustion (Figure 4-4a). The original Al NPs, viewed under the SEM, are spherical and highly agglomerated with an average diameter in the range of 60 to 96 nm (Figure 4-4b) with a 2 nm thick native aluminum oxide layer and, after flash ignition, they are oxidized into much smaller NPs (3 - 20 nm, Figure 4-8i), which are agglomerated (Figure 4-4c). It should be noted that flash ignition of Al NPs was not observed when NPs were placed sparsely over the glass slide by drop casting Al NPs diluted with hexane onto the slide and then allowing the hexane to evaporate. The above experiments suggest that particle sizes as well as the packing density are important factors for successful flash ignition.

In the case of Al MPs, optical images in Figure 4-4d show the sample appearance before and after the flash ignition in air, where the sample is a stoichiometric mixture of Al MPs (2.3 μm) and WO_3 NPs (80 nm) with $\phi = 1$. After ignition, the mixture color changes from gray to dark blue. The dark blue color indicates that WO_3 (yellow) is reduced to WO_{3-x} (blue), and not completely to W (silver or gray color). The sample is spread out over a larger area after ignition, suggesting a violent reaction that is accompanied by gas expansion. Before flash ignition, Figure 4-4e shows that the spherical Al MPs (2.3 μm) and the WO_3 NPs are mixed, forming a densely packed powder. After the flash ignition, the products form much larger particles that are tens of microns in size (Figure 4-4f), suggesting that melting and fusion occur together

with reaction. The characterizations confirm that reaction has occurred between Al MPs and WO_3 NPs upon exposure to a single optical flash. Flash ignition occurs when the energy of the incident light absorbed by the mixture of Al MPs/ WO_3 NPs is sufficient to raise the mixture temperature beyond its ignition temperature.

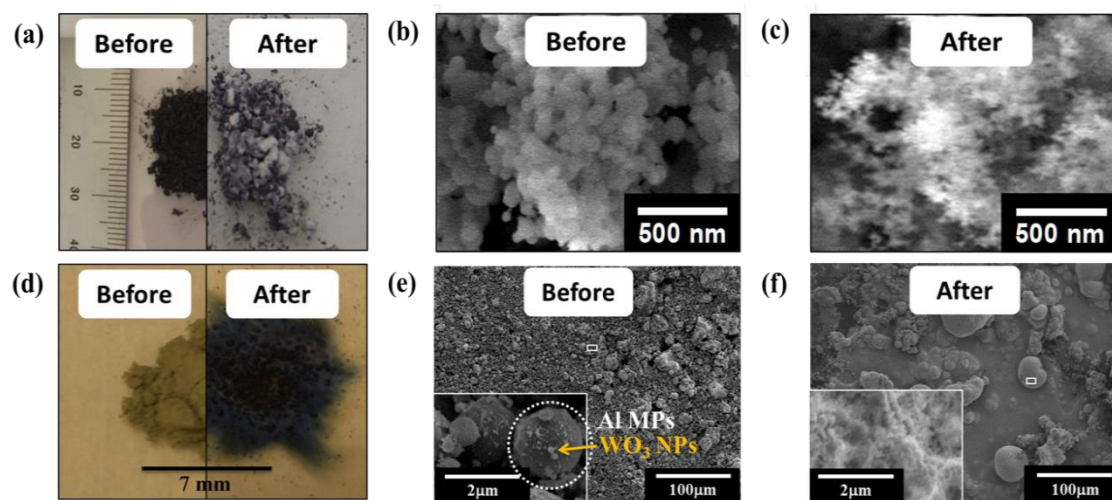


Figure 4-4: (a–c) Optical and SEM images of Al NPs before and after the exposure. The original spherical Al NPs break up into smaller clusters after burning. (d–f) Optical and SEM images of a mixture Al MPs (2.3 μm) and WO_3 NPs (80 nm). After the flash ignition, the products form much larger particles that are tens of microns in size, suggesting that melting and fusion occur together with reaction.

4.4. Material characterization of Al and WO₃ particles

4.4.1. X-ray diffraction characterization of products of Al MPs and WO₃ NPs

These micron-sized particles are further analyzed by X-ray diffraction; the dominant peaks of the XRD pattern (Figure 4-5) are those of W and Al_xWO₃, indicating that WO₃ has been reduced and some portion of it has formed aluminum-tungsten bronze. The absence of WO_{3-x} and Al₂O₃ peaks in the XRD pattern is likely because they are either amorphous or poorly crystalline. The XRD characterization confirms that the reaction has occurred between Al MPs and WO₃ NPs upon exposure to a single optical flash.

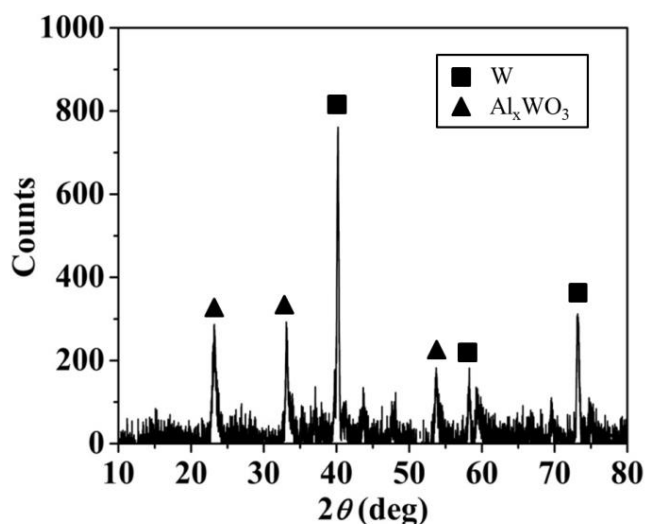


Figure 4-5: X-ray diffraction pattern of the mixture of Al MPs (2.3 μm) and WO₃ NPs (80 nm, $\phi = 1$, $\phi_n = 0.5$) after ignition.

4.5. Estimation of the temperature increase of single and multiple Al particles

To further investigate Al particle flash ignition, we estimated the temperature increase of Al particles by a single flash exposure. The flash ignition of Al NPs is achieved by the photo-thermal effect, when the energy of the incident light absorbed by Al NPs is sufficient to raise their temperatures beyond their ignition temperatures. The purpose of the calculation is to simulate the initial stage of flash ignition and to understand the qualitative dependence of temperature rise on the size and packing density of Al NPs.

4.5.1. Estimation of the temperature increase of single Al particles

First, we estimated the temperature rise from room temperature (300 K) of single isolated particles when exposed to a flash. The spectrum of the camera flash is assumed to be a blackbody radiation at a temperature of 6500 K [86] and the incident light intensity, I_{inc} , is approximately 1000 W/cm^2 on the basis of energy density of 1 J/cm^2 and the flash duration of 1 ms. [82, 87] The light absorption by the Al_2O_3 shell is neglected, since Al_2O_3 is almost optically transparent. [88] Since Al has high thermal conductivity, the temperature distribution inside the Al particle is assumed to be constant. We estimated the temperature rise of Al particles by using the heat transfer equations of a single sphere of radius R embedded in homogeneous air, where the heat source term comes from the energy absorption rate of Al NPs by the incident flash light.

$$c_{p,Al}\rho_{Al}V_{Al}\frac{\partial T_{Al}(t)}{\partial t} + 4\pi R^2 G[T_{Al}(t) - T_{air}(t, r = R)] = P \quad (3)$$

$$c_{p,air}\rho_{air}\frac{\partial T_{air}(t, r)}{\partial t} - K\nabla^2 T_{air}(t, r) = 0 \quad (4)$$

and the boundary condition is

$$K\left.\frac{\partial T_{air}(t, r)}{\partial r}\right|_{r=R} = G[T_{air}(t, r = R) - T_{Al}(t)] \quad (5)$$

, where $c_{p,air}$, $c_{p,Al}$, and ρ_{air} , ρ_{Al} are specific heat (J/kgK) and the density (kg/m³) of air and Al respectively. V_{Al} is the volume of Al; R is the radius of the particle; G is the surface conductance between the Al particle and air (MW/m²K); P is the total energy absorption rate per particle (W), and K is the thermal conductivity of air (W/mK). A finite G represents a temperature discontinuity between the interface of the particle and air. Solving for the above equations, in the limit of $t \rightarrow \infty$, the maximum temperature rise of a single particle is [87, 89]

$$\Delta T_{Al,max} = \frac{P}{4\pi R^2} \left(\frac{1}{G} + \frac{R}{K} \right) \quad (6)$$

, where $\Delta T_{Al,max}$ is the maximum temperature increase of the particle. Although the surface conductance G between the particles and air can vary from 10 to 1000 MW/m²K, [90] the corresponding final temperature only differs by 0.1 K. Hence, we neglected the contribution of G to the temperature rise in Equation (6). P is the total energy absorption rate per particle (W), which is calculated by integrating over the specific energy absorption rate over all the wavelengths λ , ranging from 200 to 1200 nm and corrected with the emissivity factor ($\varepsilon = I_{inc}/\sigma T^4$), as shown in Equation (7).

$$P = \frac{I_{inc}}{\sigma T^4} \int \frac{1}{\lambda^5} \frac{4\pi^2 c^2 \hbar}{\exp[2\pi c \hbar / (\lambda k_B T)] - 1} C_{abs}(\lambda) d\lambda \quad (7)$$

, where σ is the Stefan–Boltzmann constant; c is the speed of light; \hbar is the reduced Planck constant, and k_B is the Boltzman constant. The specific energy absorption rate at a specific wavelength is the product of the absorption cross-section, $C_{abs}(\lambda)$, and the intensity of the incident light at the wavelength. The absorption cross-section $C_{abs}(\lambda)$ was calculated by using a Mie theory calculator “Mieplot”. [91] The estimated temperature rises of single Al particles with diameters of 70 nm and 20 μm are 0.18 K and 197 K respectively, and both final temperatures are much lower than the typical ignition temperature of Al NPs, which ranges from about 833 K to the melting point of Al (933 K). [92-94] This result is consistent with our experimental observation that sparsely dispersed Al NPs and large MPs are not ignited by a xenon flash.

4.5.2. Estimation of the temperature increase of multiple Al particles

Hence, it is necessary to consider the effect of multiple Al particles, the packing density, for which we define the packing density as $\phi = V_{Al}/V_{air}$, i.e., the volume ratio of Al particles to the confined air among the particles. The temperature rise of Al particles was estimated by assuming that the energy absorbed by the Al particles is used to heat up the particles and the confined air. [87]

$$(\rho_{air} V_{air} c_{p,air} + \rho_{Al} V_{Al} c_{p,Al}) \Delta T = p V_{Al} \Delta t, \quad (8)$$

$$\Delta T = \frac{p \Delta t}{\frac{\rho_{air} c_{p,air}}{\phi} + \rho_{Al} c_{p,Al}} \quad (9)$$

, where p is the energy absorption rate per unit volume (W/m^3) by Al, and Δt is the flash duration (sec). Here for estimation purpose, we assumed that the Al and air have the same temperature rise, although the actual temperature of Al will be higher than that of air. [95] We also neglected the optical interactions among Al particles and the possible air expansion between Al NPs due to the heating. It should be noted that the estimation presented here is not a rigorous flash heating model, which is far from trivial due to the complexity in describing the Al NP distribution and interfacial heat conductivity, but rather its purpose is to provide qualitative information on the dependence of temperature rise on the size and packing density of Al NPs.

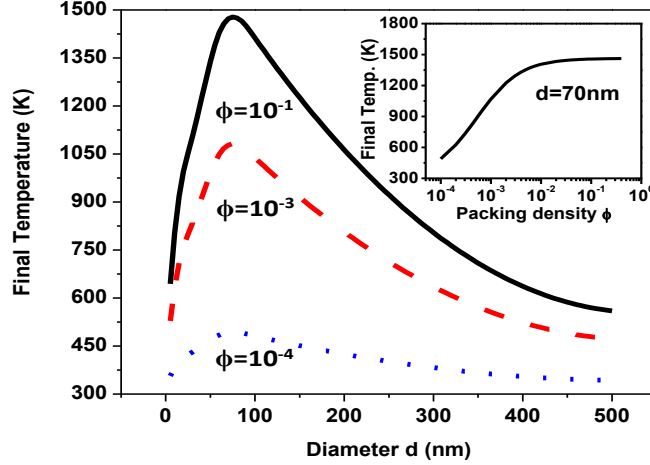


Figure 4-6: Estimated temperature rise of Al particles by a flash exposure as a function of the Al particle diameter for different packing densities. Inset: The temperature rise of Al NPs with a diameter of 70 nm as a function of the packing density of Al NPs.

Figure 4-6 shows the dependence of the temperature rise of the Al particles on their sizes and packing densities. First, the largest temperature rise is expected for Al particles with approximately 75 nm diameter, regardless of the packing density. As the size of the Al particles increases beyond 75 nm, the temperature rise decreases because the particles absorb less energy. In addition, larger micron Al particles require much higher ignition temperature of above 1200 K. [92] Hence, large Al MP alone cannot be ignited by a flash. Second, there is a critical Al packing density to achieve flash ignition because, for Al particles of the same diameter, their temperature rise increases sharply with the Al packing density and eventually saturates when the packing density is roughly above 1% (Figure 4-6, inset). The reason that higher temperature rise is expected for larger packing densities of Al particles is that more heat per unit volume is absorbed. In summary, successful flash ignition of Al particles relies on two important parameters: their diameters and their packing densities

4.6. Al nanoparticle oxidation mechanism

Next, we investigated the oxidation mechanism of Al NPs ignited by a camera flash. Al NPs ignited by the flash are likely to be oxidized by the MDM due to the large heating rate, on the order of 10^6 K/s or higher. To verify the Melt-Dispersion Mechanism (MDM) oxidation, Al NPs were first exposed to the flash in an inert Ar gas to avoid further oxidation. During the flash exposure, no ignition was observed and the remaining Al NPs were collected for TEM characterization. The TEM images (Figure 4-7a and inset) show that Al NPs have average diameters of 60 - 96 nm and roughly 2

nm thick Al_2O_3 shells before the flash exposure. After the flash exposure, the Al_2O_3 shell is partially ruptured and the molten Al is dispersed out of the shell (Figure 4-7b and c). The observation suggests that the flash provided enough energy to melt the Al and generated a large dynamic pressure inside the NP to rupture its shell, and eventually led to the outflow of the molten Al.

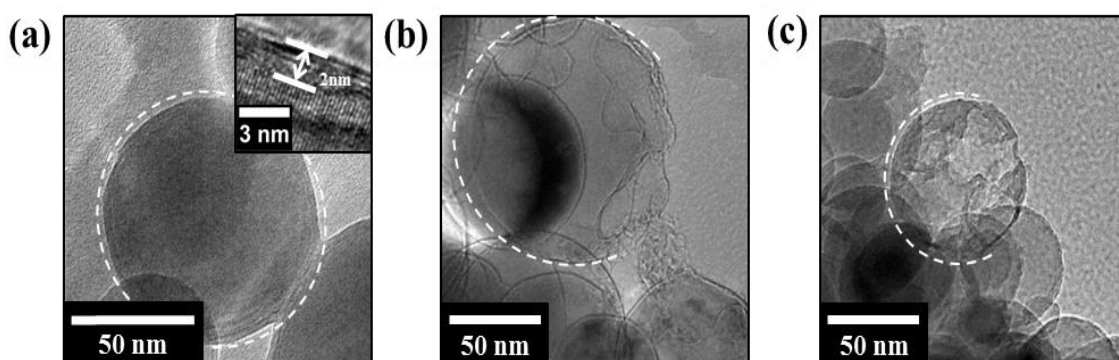


Figure 4-7: Exposure of Al NPs to a flash in Ar. a) TEM image of the Al NPs before flash exposure. Inset: the Al NP is covered by an alumina shell about 2 nm thick. b) and c) TEM images of two different Al NPs after flash exposure in Ar showing that both alumina shells have ruptured after the flash exposure.

We further studied the oxidation process of Al NPs in air by examining multiple NPs after the flash exposure using TEM. Due to the intrinsic spatial non-uniformity of the flash light intensity and the packing density of Al NPs, Al NPs will have different temperature rise and exposure to oxygen, so their oxidation process will quench at different stages after the flash exposure. Therefore, by examining many Al NPs, we can re-construct the oxidation process of Al NPs as illustrated in Figure 4-8. Initially,

similar to the case in Ar, Al melts upon exposure to the flash, which pushes the oxide shell outwards (Figure 4-8b and f). When the pressure rise associated with the melting of Al is large enough, it ruptures certain regions of the oxide shell and the molten Al flows out (Figure 4-8c and g). Subsequently, Al and oxygen contact with each other and react exothermically. The heat generated further causes more Al to melt or even evaporate, which pushes the oxide shell further out, and the original Al NP has grown from less than 100 nm to over 300 nm in diameter (Figure 4-8d and h). As shown in Figure 4-8h, the big hollow sphere corresponds to the expanded Al particle and the much smaller solid spheres formed from the core Al remains inside the hollow sphere. Eventually, the entire particle fractures and breaks into clusters of 3 - 20 nm, much smaller than the original Al NPs (Figure 4-8e and i). The clusters consist of both Al_2O_3 particles and partially oxidized Al particles. These observations strongly suggest that the Al NPs ignited by the flash are oxidized by the MDM.

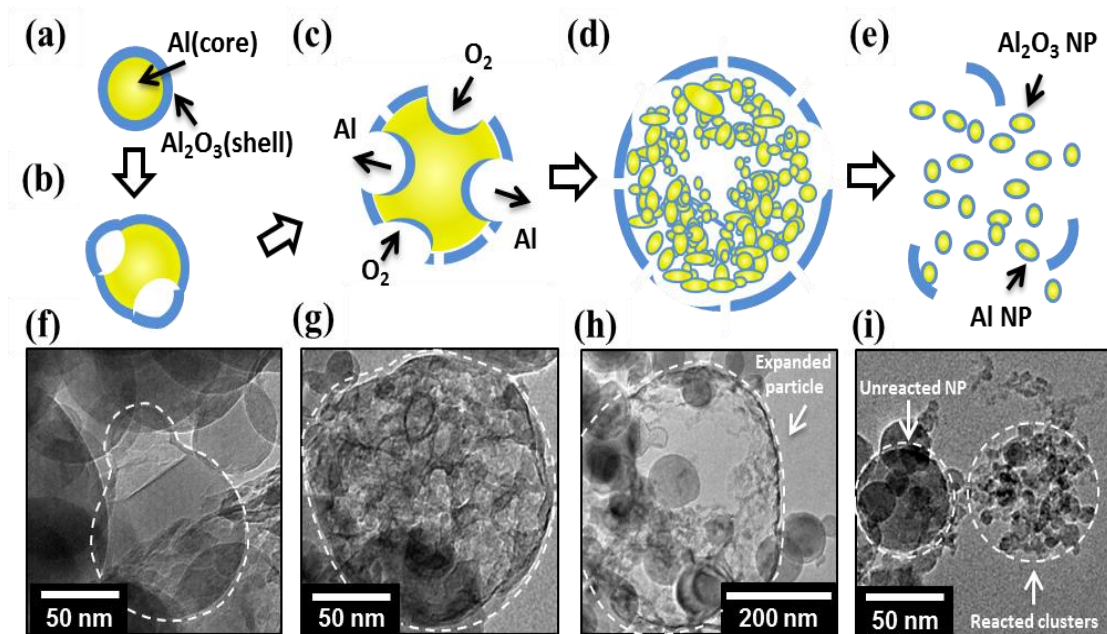


Figure 4-8: (a - e) Schematics and (f - i) TEM images illustrate the oxidation process of the Al NPs when exposed to a flash in the air. a) Initial Al NPs are covered by a Al_2O_3 shell. b) and f) Al melts upon rapid heating which pushes the shell outward. c) and g) the shell ruptures and the melted Al becomes in contact with air. d) and i) the large hollow sphere corresponds to the expanded Al NPs, where most Al has flown away from the particle center and been oxidized at the particle surface. e) and j), the hollow sphere fractures into small clusters of 3 – 20 nm in sizes. These clusters are consisted of both Al_2O_3 particles and partially oxidized Al particles.

4.7. Reducing minimum flash ignition energy of Al microparticles by addition of WO₃ nanoparticles

4.7.1. Minimum flash ignition energy of the mixture of Al MPs and WO₃ NPs

We then extended the flash ignition from Al NPs to Al MPs by the addition of WO₃ NPs. WO₃ NPs influence the flash ignition of Al MPs in two ways: (1) increasing light absorption and (2) decreasing ignition temperature by supplying oxygen to Al. To quantify the effect of WO₃ NPs, the E_{min} for the mixture of Al MPs and WO₃ NPs is plotted as a function of normalized Al/WO₃ equivalence ratio in both air (black squares) and inert N₂ (red circles) in Figure 4-9. The E_{min} of each sample is determined by increasing the power of the flash until ignition occurs. Figure 4-9a and b correspond to larger Al MPs (2.3 μ m) and smaller Al MPs (0.9 μ m), respectively. The error bar represents the standard deviation of the E_{min} . First, both E_{min} curves (Figure 4-9a and b) show a concave shape, with higher E_{min} values in both the Al lean and rich regions, a trend that is very similar to that of E_{min} for ignition of various gaseous fuel/air mixtures. [96] The lowest point of the E_{min} curve does not correspond to the stoichiometric condition of reaction $2\text{Al} + \text{WO}_3 \rightarrow \text{Al}_2\text{O}_3 + \text{W}$ ($\phi = 1$, $\phi_n = 0.5$), since WO₃ is not completely reduced to tungsten in the flash experiment. Second, when Al is the deficient species with respect to WO₃ ($\phi_n < 0.5$), E_{min} in the air is comparable to that in N₂. The fact that E_{min} does not increase when gaseous O₂ is removed suggests that Al MPs are preferentially oxidized by the WO₃ NPs. WO₃ NPs are more effective oxidizers than air because of their large contact area with the Al MPs, which facilitates ignition through the diffusion-based reactive sintering mechanism. [97, 98] Third, adding WO₃

NPs to pure Al MPs ($\phi_n = 1$) or to Al MPs in excess supply with respect to WO_3 ($\phi_n > 0.5$), *i.e.*, changing ϕ_n from 1 to 0.5, significantly lowers E_{min} because WO_3 oxidizes Al more effectively than air. Finally, when comparing Al MPs of two different sizes, E_{min} for the 2.3 μm Al MPs is on average 0.4 J/cm^2 higher than that for the 0.9 μm Al MPs, which is consistent with the reported observation of higher ignition temperature of 1600 K for larger (2.3 μm) particles compared to 1400 K for smaller (0.9 μm) particles. [10, 12] Nevertheless, the addition of WO_3 NPs reduces E_{min} for Al MPs of both sizes.

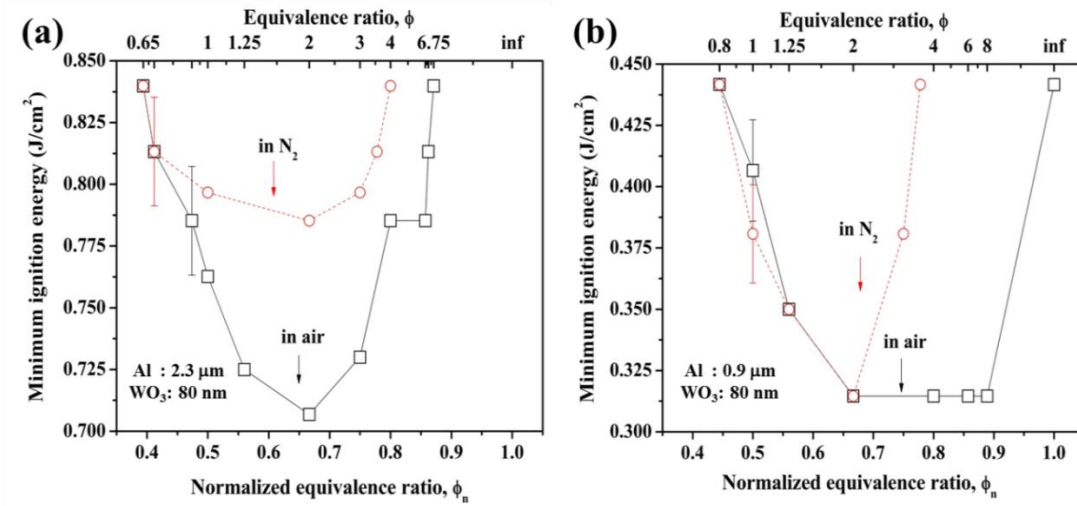


Figure 4-9: Minimum flash ignition energy of Al MPs with addition of WO_3 NPs. a) Large Al MPs (2.3 μm) and b) small Al MPs (0.9 μm) mixed with WO_3 NPs with respect to normalized equivalence ratios in air and nitrogen gas.

4.7.2. Optical characterizations of Al MPs with addition of WO_3 nanoparticles

The wavelength-dependent light absorption properties of various mixture samples are obtained with an integrating sphere using a xenon lamp coupled to a

monochromator (Model QEX7, PV Measurements, Inc.). For the reflectance (R %) measurement, the samples are mounted at the backside of the integrating sphere and the reflectance spectra are normalized to the reflection of a white-standard. The transmittance spectra (T %) are obtained by comparing the transmittance of test samples with a calibrated Si reference photodiode. The absorption (A %) is calculated with the formula, $A \% = 100 \% - T \% - R \%$.

The above E_{min} measurements show that WO_3 NPs are more effective oxidizers than air for Al MPs. In addition, WO_3 NPs can also enhance the light absorption of the mixture of Al MPs/ WO_3 NPs upon flash exposure, which can increase the temperature rise due to the photothermal effect.

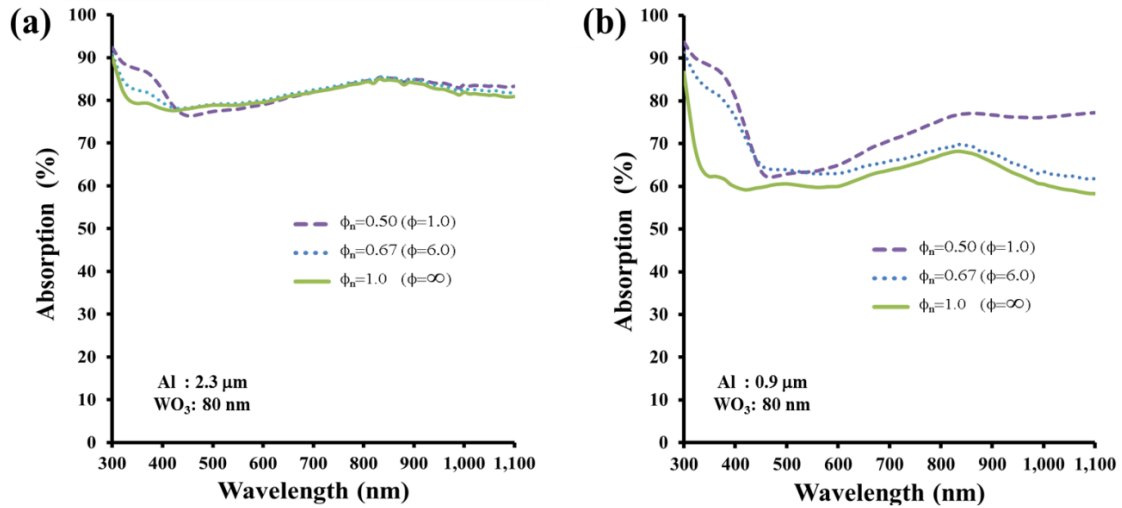


Figure 4-10: Optical characterizations of Al MPs with addition of WO_3 NPs. Absorption a) large Al MPs (2.3 μm) and b) small Al MPs (0.9 μm) mixed with WO_3 NPs with respect to normalized equivalence ratios over a wavelength of 300 - 1100 nm.

Figure 4-10 shows the light absorption spectra of several mixtures of Al MPs and WO₃ NPs over wavelengths of 300 - 1100 nm. Figure 4-10a and b correspond to larger (2.3 μm) and smaller (0.9 μm) Al MPs, respectively. First, for pure Al MPs ($\phi_n = 1.0$), the slight absorption increase around 830 nm corresponds to the inter-band transition frequency of 1.5 eV for aluminum. [99] For all the other samples containing WO₃ NPs, light absorption is clearly increased for wavelengths below 460 nm, consistent with the WO₃ bandgap of 2.7 eV ($\lambda = 460$ nm). Second, the smaller Al MPs absorb about 15 % more light than the larger Al MPs, facilitating the flash ignition process. Third, the total light absorption is calculated by integrating the product of the xenon flash spectrum and the absorption plus scattering spectrum over 300 - 1100 nm wavelengths. The total light absorption is increased by 12.2 % and 1.4 % for the larger (2.3 μm) and smaller (0.9 μm) Al MPs, respectively, when a stoichiometric quantity of WO₃ NPs ($\phi_n = 0.5$) is added to the pure Al MPs. Since the light absorption enhancement due to the addition of WO₃ NPs is negligible for the smaller Al MPs, the reduction in E_{min} is mainly attributed to effective oxygen supply by WO₃ NPs due to their intimate and large contact area with Al MPs. On the other hand, for larger Al MPs, the reduction of E_{min} by WO₃ addition results from both effective oxygen supply and enhanced light absorption.

4.8. Conclusion

We have demonstrated that Al NPs and MPs can be ignited by a xenon flash through the photo-thermal effect. Flash ignition has the advantages of low power input,

multi-point initiation and broad spectrum emission. Our analysis reveals that successful flash ignition requires Al particles to have a suitable submicron diameter range and a large packing density, in order to achieve sufficient temperature rises. Furthermore, TEM analysis of Al NPs after the flash exposure in the air suggests that Al NPs are oxidized through the Melt-Dispersion Mechanism, which is the first direct experimental observation thereof. We also have extended the flash ignition from Al NPs to Al MPs and studied the effect of WO₃ NP addition on the flash ignition of Al MPs of two different sizes by measurement of the E_{min} . The E_{min} is greatly reduced by the addition of WO₃ NPs for Al MPs of both sizes. For the smaller Al MPs, the reduction mainly comes from more effective oxygen supply by WO₃ NPs than by air. For the larger Al MPs, the reduction is due to the combined effects of effective oxygen supply and light absorption enhancement by WO₃ NPs. These results extend the flash ignition of expensive and lower energy density Al NPs to inexpensive and higher energy density Al MPs. The flash ignition may find uses in many engineering applications requiring distributed, nonintrusive and miniaturizable ignition systems in lieu of sparks and hotwire igniters.

5. Flash ignition of freestanding porous Si film

Chapter 4 introduces the flash ignition of Al particles investigating the requirements for successful flash ignition with respect to both the fuel and oxidizer. In this Chapter, we extend the flash ignition to freestanding porous Si film and explain the important parameters that control the minimum flash ignition energy of the porous Si film in ambient air.

5.1. Background

Understanding the ignition properties of porous Si is of great practical importance to reliably initiate the controlled combustion of porous Si and to prevent unwanted combustion for safety reasons. Various ignition methods, such as mechanical fracture [31], laser [100] and hotwire [101] have been applied to initiate the combustion of porous Si. However, optical ignition with a light source containing a broad band of wavelengths, such as a xenon flash lamp, has not been reported. Flash ignition is practically convenient because it is non-intrusive, low-cost and can achieve distributed ignition of energetic materials to enhance the energy release rates. [80, 82, 84, 102-105]

In this study, we report the first successful flash ignition of freestanding porous Si films in ambient air and investigate the effects of film thickness and porosity on the

minimum flash ignition energy (E_{min}) with combined experimental and numerical studies. The E_{min} is of great importance when handling, storing and applying porous Si to energetic applications. We find that the E_{min} decreases with decreasing the film thickness and increasing the film porosity.

5.2. Flash ignition of porous Si film

5.2.1. Experimental setup and flash ignition process of Si film

Analogous to the flash ignition of Al particles, the experimental setup for flash ignition of porous Si film is schematically illustrated in Figure 5-1a.

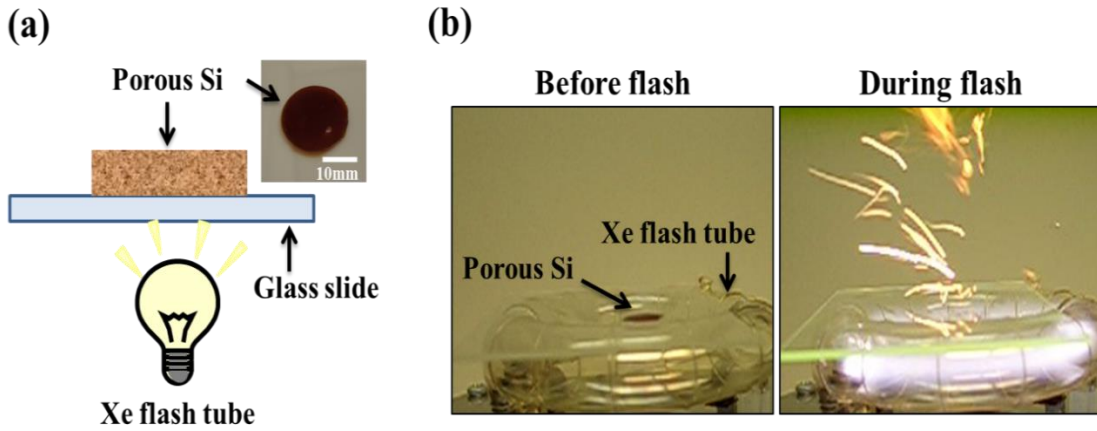


Figure 5-1: (a) Schematic of the experimental setup for the ignition of freestanding porous Si films by a xenon flash. (b) Optical images of a freestanding porous Si film before and during the xenon flash exposure.

The porous Si film is placed on top of a 1 mm thick glass slide directly above the xenon flash tube [104] as shown in Figure 5-1b (left image). Once the flash is triggered, the porous Si film ignites, propels vertically, and burns violently in air in a fraction of a second (Figure 5-1b, right image). The dynamic flash ignition process of the freestanding porous Si film is recorded by the high speed camera (FASTCAM SA5, Photron USA, Inc), equipped with a macro lens for enhanced spatial and temporal resolution. Figure 5-2a shows the unreacted porous Si film as indicated by the dash line, which is placed on top of the xenon flash tube.

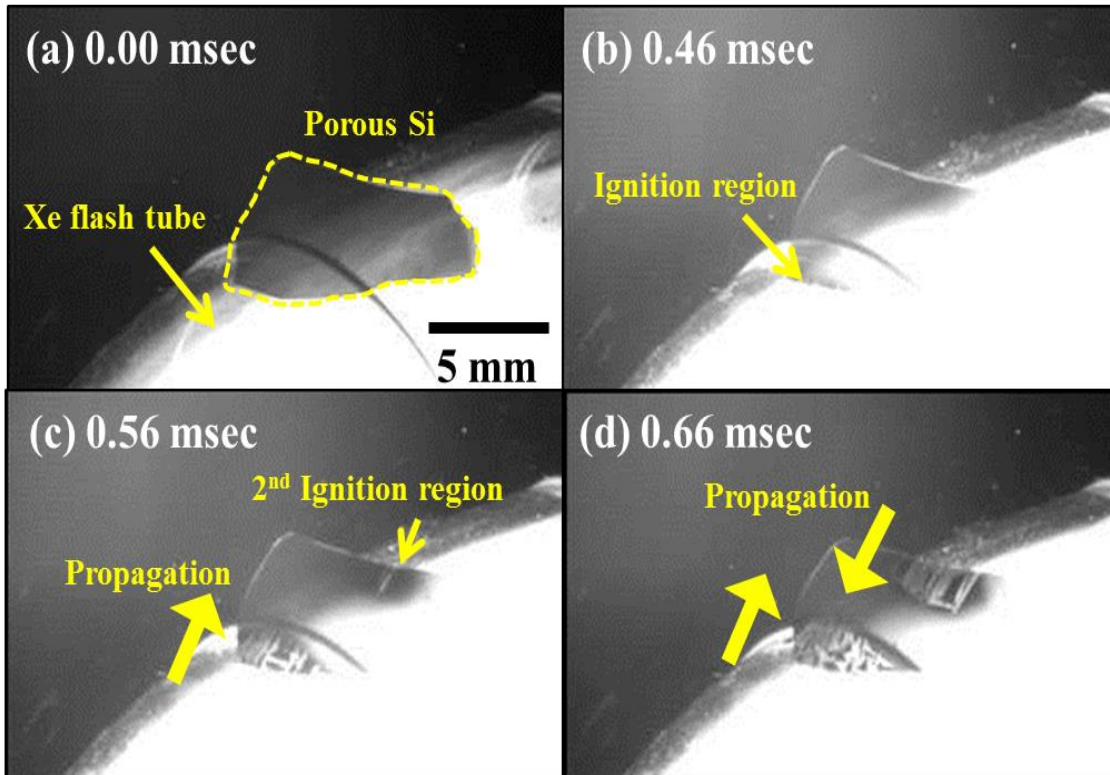


Figure 5-2: High speed camera images capturing the ignition and combustion process of a freestanding porous Si film when exposed to the xenon flash. The porous Si film

ignites at multiple locations and the reaction front propagates from the ignition region into the unreacted porous Si regime.

At $t = 0.46$ msec after exposing the porous Si film to the xenon flash, ignition is observed along the front edge of the film (Figure 5-2b). At $t = 0.56$ msec (Figure 5-2c), the ignition region has propagated from the front edge towards the middle part of the film, as evidenced by the observed fragmented film. At the same time, another ignition is initiated near the back edge of the film and also propagates towards the middle of the film at $t = 0.66$ msec (Figure 5-2d). Upon further propagation, the porous Si film is propelled upward from the underlying glass slide and burns violently in air. It should be noted that the nonuniform ignition for the porous Si film is due to the curvature of the xenon flash tube, which leads to slightly varying distance between different parts of the porous Si film to the xenon lamp.

5.2.2. Minimum flash ignition energy of porous Si film

An important parameter for practical application of flash ignition of porous Si is the minimum ignition energy (E_{min}). When the porous Si film absorbs enough light to raise the temperature beyond its ignition temperature, flash ignition occurs. The ignition temperature of the porous Si in air is in the range of 500 - 580 K in air, [23] at which the surface Si-H bonds of the porous Si breaks and the exposed Si atoms react with oxygen, leading to ignition. The typical porous Si sample dimension for the E_{min} experiment is about a couple of millimeters, which is much smaller than the diameter of the xenon

lamp tube (15 mm), so that the incident light intensity on the entire sample can be assumed to be uniform. Here, we investigate the dependence of E_{min} on controlling two parameters: 1) film thickness and 2) porosity, because both parameters affect the optical absorption, [106] thermal conductivity [107-109] and combustion properties [25] of porous Si. Freestanding porous Si films with different thickness and porosity are prepared by varying the electrochemical etching time and the HF/ethanol volume ratio. The film thickness is increased by increasing the etch time. The porosity is increased by decreasing the HF/ethanol volume ratio [61] and the porous Si films with low/intermediate/high porosities are respectively prepared by etchants with the HF/ethanol volume ratios of 1:0.5, 1:0.75, 1:1. It should be noted that the porosity also increases with increasing the etch time, correspondingly with increasing the film thickness. Hence, it is necessary to study the effect of porosity by comparing films of the same thickness.

The E_{min} of freestanding porous Si films are plotted as functions of film thickness and porosity in Figure 5-3. It is clearly seen that the E_{min} increases with increasing the film thickness and decreasing the film porosity.

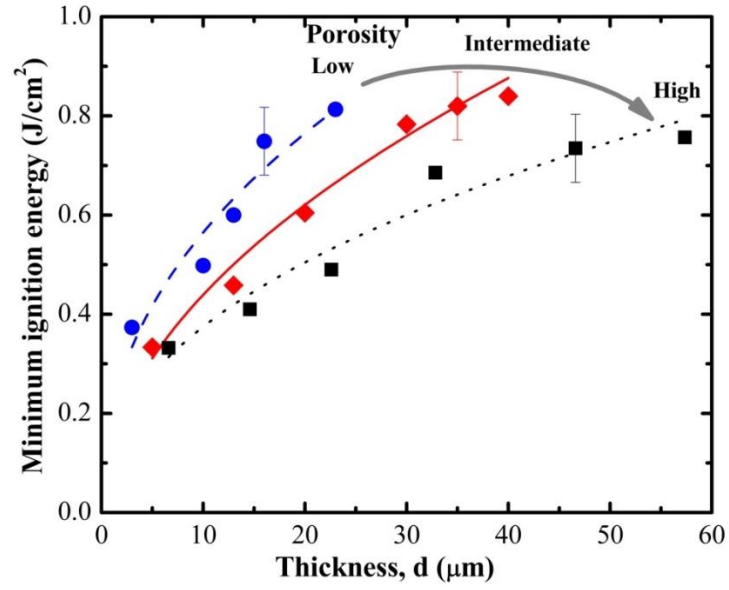


Figure 5-3: Experimentally measured minimum flash ignition energies of freestanding porous Si films as functions of film thickness and porosity. The error bar represents the standard deviation of the E_{min} .

5.2.3. Estimation of the temperature increase of a porous Si film

To understand the observed dependence of the E_{min} on the film thickness and porosity, we calculate the dynamic temperature profiles within the porous Si film due to a single flash exposure using the COMSOL Multiphysics software. Specifically, the numerical simulation schematic is set up on the basis of our experimental configuration (Figure 5-1a) and it consists of a porous Si film on top of a 1 mm thick glass slide with a pulse of heat supplied from the bottom of the glass slide (Figure 5-4).

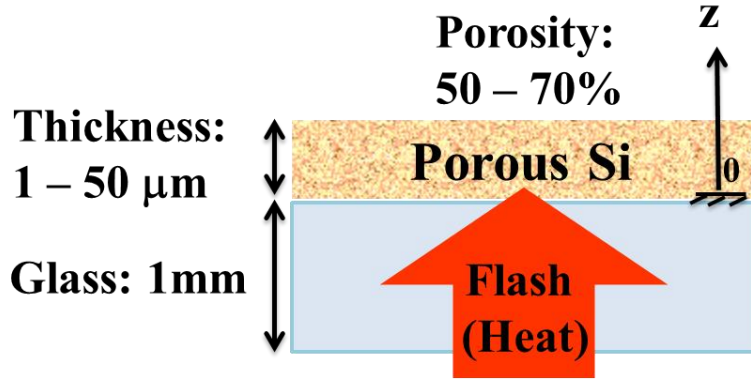


Figure 5-4: Schematic of the numerical setup for calculating the temperature rise of a freestanding porous Si film by the xenon flash.

We assume that this is a one-dimensional time dependent heat transfer problem in solids. The heat provided by the xenon lamp is mainly absorbed by the porous Si according to the Beer-Lambert Law, not by the glass slide due to its high transparency. The porous Si simultaneously loses heat to the bottom glass slide due to heat conduction and air due to natural convection. The incident xenon flash is simplified into a single wavelength light source at 450 nm, where the xenon flash intensity peaks. The output power density-time profile of the single flash pulse output is modeled by a Gaussian function as

$$I_0(t) = \frac{E}{\tau} \exp \left[\frac{-(t - \tau)^2}{2\tau^2} \right] \quad (10)$$

, where $I_0(t)$ (W/m^2) is the output power density of the flash, E is the pulse energy (J/m^2), and τ is set to be 0.5 msec to simulate the xenon pulse time. The spatial and

temporal temperature profiles within the porous Si and glass are described by a one-dimensional unsteady heat transfer equation

$$\rho c_p \frac{\partial T}{\partial t} = \alpha(1 - R)I_0(t)e^{-\alpha z} + \frac{\partial}{\partial z} \left(k \frac{\partial T}{\partial z} \right) \quad (11)$$

, where T is the temperature (K), and ρ , c_p , k , and α are the density (kg/m^3), specific heat ($\text{J/(kg}\cdot\text{K)}$), thermal conductivity ($\text{W/(m}\cdot\text{K)}$), and absorption coefficient (m^{-1}) at 450 nm of the porous Si for $z \geq 0$ and glass slide for $z < 0$, respectively. The absorption coefficient (α) for the glass is set to be zero, since the glass is almost transparent. R is the reflectivity of porous Si at 450 nm and is set to be 0.1. [110, 111] The density of the porous Si is calculated by $\rho_{p-Si} = \rho_{bulk-Si}(1 - \text{porosity})$. [109] The initial and boundary conditions are expressed as:

$$T(z, t = 0) = 300\text{K}; \quad T(z = -1\text{mm}, t) = 300\text{K}; \quad k \frac{\partial T}{\partial z} \Big|_{z=d} = h(300\text{K} - T(d, t)) \quad (12)$$

, where d (μm) is the total thickness of the porous Si film, and h is the convective heat transfer coefficient of ambient air ($5 \text{ W/(m}^2\text{K)}$). In COMSOL, the temperature profiles of porous Si films are simulated using the Heat Transfer in Solids Module. The material parameters for the silica glass, bulk Si, and air are obtained from the COMSOL material library. The physical properties of porous Si are referred from literature values (Table 3).

Table 3: Parameters and values of porous Si used in the COMSOL simulation.

Parameters	Values	Refs
Specific heat of porous Si, C_{p-Si} (J/(kgK))	$35.6 \cdot (24 + 0.003 \cdot T - 4.23 \cdot 10^{-5} / T^2)$	[112]
Absorption coefficient of porous Si, α (m^{-1}) (Porosity = 50%, 60%, 70)	1338200, 929300, 682700	Average values from [107, 113-115]
Thermal conductivity of porous Si, k_{p-Si} (W/mK) (Porosity = 50%, 60%, 70)	0.422, 0.352, 0.302	Average values from [107-109]

A representative temperature history of the porous Si film is shown in Figure 5-5 for which the film is specified with a thickness d of 20 μm , porosity of 70 %, and pulse energy E of 700 mJ/cm^2 .

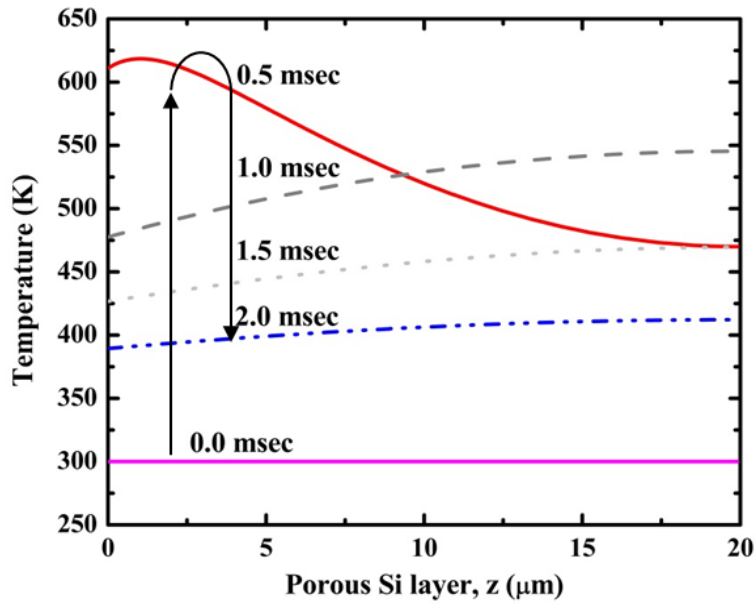


Figure 5-5: Calculated time-dependent temperature profile within the freestanding porous Si film.

Initially at $t = 0$ msec, the entire porous Si film is at room temperature (300 K). At $t = 0.5$ msec immediately after the flash pulse, the temperature at the bottom of the porous Si layer rises above 600 K, which is higher than the ignition temperature (500 - 580 K) of porous Si in the air. [23] The temperature is lower at higher z values (further away from the flash) since the amount of light absorption drops exponentially with distance. Once the flash pulse is over ($t = 1.0 - 2.0$ msec), the temperature of the porous Si gradually returns to the room temperature due to heat losses to the glass slide and ambient air.

The calculated maximum temperature of the porous Si film due to flash heating is plotted as functions of the porous Si film thickness and porosity (Figure 5-6).

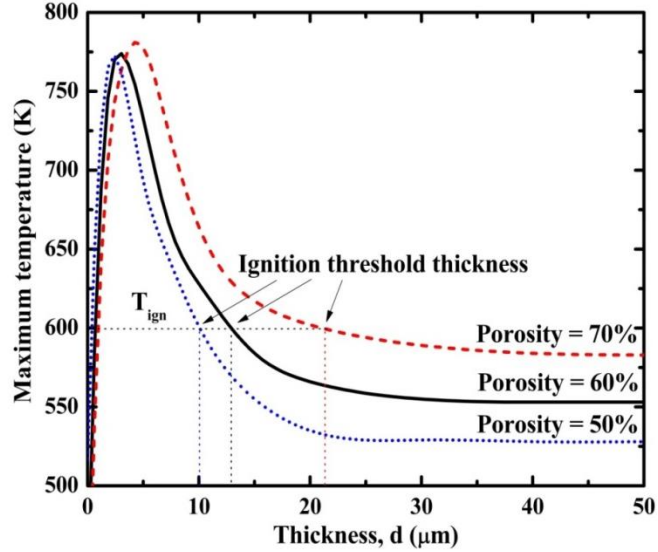


Figure 5-6: Calculated maximum temperature rise of freestanding porous Si films by the xenon flash as functions of film thickness and porosity.

Here, the thickness and porosity are varied between 1 – 50 μm , and 50 – 70 %, while the pulse energy density E is fixed at 700 mJ/cm^2 . First, the largest temperature rise is observed for porous Si film about 5 μm in thickness. Below 5 μm , the porous Si is too thin to absorb all the incident light, resulting in a low temperature rise. Above 5 μm , the additional porous Si thickness serves as a heat sink since the first ~ 5 μm absorbs the majority of the light, again lowering the temperature rise. Second, the maximum temperature rise is slightly higher for higher porosity Si since it loses heat slower due to lower thermal conductivity (Table 3). The optimal thickness for the highest temperature rise is slightly larger for higher porosity because it has a smaller light absorption coefficient. Third, the effect of porosity becomes more prominent for thicker porous Si films. As seen in Figure 5-6, the temperature rise is similar at smaller thickness but grows larger at larger thickness for the three Si films of different porosity. For thicker porous Si films, high porous film has much smaller heat capacity ($\rho_{p-Si}Cp_{p-Si}$) and lower thermal conductivity leading to large temperature rise. Finally, the minimum ignition energy E_{min} is plotted as functions of thickness and porosity of the porous Si films in Figure 5-7 in order to compare with our experimental results.

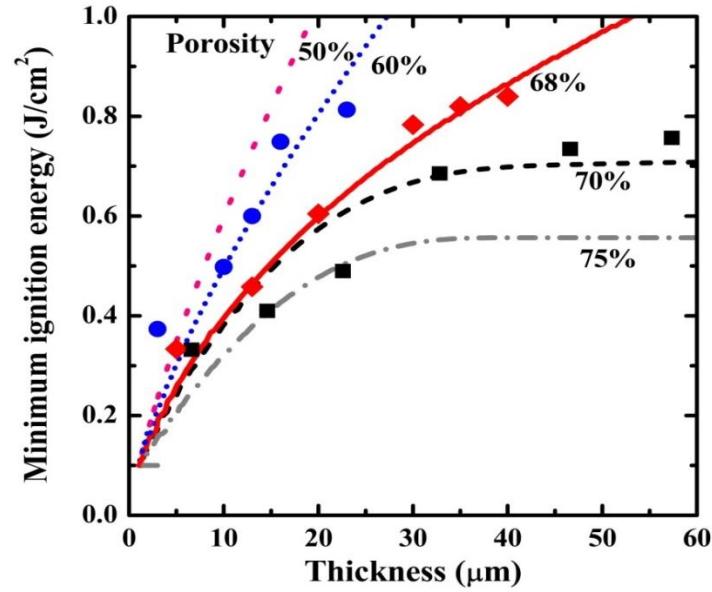


Figure 5-7: Calculated minimum flash ignition energy density for freestanding porous Si films by the xenon flash as functions of film thickness and porosity.

For qualitative comparison purpose, we define ignition numerically as long as the peak temperature of the porous Si exceeds 600 K. The plot is generated by calculating the threshold film thickness, at which the maximum temperature reaches 600 K, for each fixed incident energy level and porosity. Similar to the observations made from Figure 5-6, the E_{min} increases with increasing the film thickness and decreasing porosity. The E_{min} is more sensitive to the porous film thickness when it is less than 25 μm . The E_{min} is more sensitive to the film porosity for thicker porous Si films, for which the E_{min} difference among three different porosities becomes bigger for thicker films. These findings are consistent with the experimental results (Figure 5-3).

5.3. Conclusion

To summarize, we have demonstrated that freestanding porous Si films can be optically ignited in ambient air by a low power xenon flash ($< 1 \text{ J/cm}^2$) through the photothermal effect. Flash ignition occurs when porous Si absorbs enough energy to raise its temperature beyond its ignition temperature. Our complementary experimental and numerical studies reveal that the minimum flash ignition energy increases with increasing the thickness due to heat loss through the porous Si layer. The minimum flash ignition energy is lower for higher porosity Si film because higher porosity reduces the heat capacity and thermal conductivity, facilitating the temperature rise. We believe that these results will be of great importance to reliably initiate controlled porous Si combustion and to prevent unwanted combustion for practical application of porous Si as energetic materials.

6. Conclusion

Al and Si have broad applications in propulsion, thermal batteries, waste disposal, and power generation for micro systems as energetic materials. The advantage of large volumetric energy densities, earth abundance, and low cost are desirable properties for energetic materials. However, the slow energy release rates and the high ignition temperatures cause difficulty in tailoring the combustion performance to targeted applications. Recently, reducing the sizes of energetic materials down to the nanoscale has been reported to be effective in increasing their reaction rates and reducing their ignition temperature. Therefore, this dissertation focuses on two areas of Al and Si-based energetic materials: 1) the effects of the nanostructured morphology on the exothermic reaction, 2) demonstrate and understand the flash ignition of Al NPs, and extending the flash ignition to Al MPs and porous Si films.

To overcome the challenges in preparing energetic materials with nanoscale uniformity, we synthesize energetic materials that achieve excellent spatial uniformity in the form of the core/shell structure and freestanding porous Si film. The synthesis of the CuO/Al core/shell structured NWs was conducted by growing CuO NWs via annealing of copper and depositing a layer of Al by magnetron sputtering. The synthesis of core/shell particles was realized by coating the Al particles with a very thin CuO

shell using a solution phase method. The large yield of sample mass synthesized by the solution phase method enables to measure the run burning rate. Both core/shell NW-based and particles-based Al/CuO composite have excellent chemical homogeneity between fuel and oxidizer in a united structure. We have determined the exothermic onset temperatures and heat release characteristics of energetic CuO/Al core/shell structures for both NWs and particles through DSC measurements. The exothermic onset temperature of the core/shell NWs is unaffected to the Al layer thicknesses. The core/shell NWs, compared to the powder of NPs, has no endothermic peak associated with residual Al melting in the heat release profile and exhibit reduced activation energy for the thermite reaction between CuO and Al. Furthermore, for core/shell particles, the intimate contact area between Al and CuO has a small effect on onset temperatures and the burning rate measurements showed much larger propagation speed than those of the mixture of Al and CuO NPs. The core/shell structure and the synthesis the methods can be applied to other metal and metal oxide shells, to achieve excellent spatial uniformity, and large reactivity. These observations suggest the great potential of core/shell structure thermites and open up more opportunities to develop a more efficient united fuel and oxidizer nanostructures.

Second, we have demonstrated that Al NPs, MPs and porous Si films can be ignited by a low power ($1 < J/cm^2$) xenon flash through the photothermal effect. The nonintrusive optical flash ignition is attractive due to its low power input, multi-point initiation, and flexibility in controlling the area exposed to the flash. For Al NPs, in

order to achieve sufficient temperature rise to successfully flash ignite Al particles, the Al particle should have a suitable submicron diameter and an adequate packing density. TEM analysis suggests that the flash ignited Al NPs are oxidized through the Melt-Dispersion Mechanism. For Al MPs, we studied the effect of WO₃ NP addition on the flash ignition of Al MPs with two different sizes ($d = 0.9\ \mu\text{m}$, $2.3\ \mu\text{m}$) and the minimum flash ignition energies for both sizes are reduced by the addition of WO₃ NPs. In the case of small Al MPs, the reduction is attributed to the effective oxygen supply by WO₃ NPs. In the case of large Al MPs, the reduction results from both the effective oxygen supply and light absorption enhancement by WO₃ NPs. Finally, for freestanding porous Si films, we identified two physical parameters (film thickness and porosity) that affect the minimum flash ignition energy of porous Si film. Both experimental and numerical analyses suggest that the minimum flash ignition energy increases by increasing the film thickness and decreasing the porosity. The excess thickness contributes to heat loss through the porous Si layer, and the low porosity increases the heat capacity and thermal conductivity. These flash ignition study support to prevent from unexpected ignition of porous Si films for safety reasons and demonstrates to reliably ignite energetic materials that could be applied to engineering applications requiring nonintrusive, and distributed ignition systems.

7. Recommendation for future work

In this chapter, we propose two classes of future work: time-resolved measurements for studying oxidation kinetics between Al and metal oxide using a micro-thermal stage, and the engineering application for flash ignition of porous Si.

7.1. Oxidation kinetics studies of thermite mixtures using the Micro-Thermal Stage

Current knowledge of oxidation of Al particle originates from global reaction characteristics, such as ignition temperatures and flame propagation speeds. We have studied the performance of core/shell structured energetic materials and the role of the WO_3 NP upon flash ignition, however, the detailed oxidation reactions and kinetics at the interface of Al and metal oxides remain unresolved under fast heating rate (10^6 K/s \sim). The Al could dynamically evolve at sub-millisecond time scale, a time regime difficult to access, so those global behaviors offer very limited information on the detailed reaction process, preventing testing the validity and applicability of different theories (e.g., diffusion and melt-dispersion). The recommend future work is to conduct time-resolved measurement of the detailed dynamic changes of condensed phases at sub-millisecond time scale. We will design and fabricate a micro-thermal stage (MTS) that has a wide heating rate range up to 10^7 K/s and a thermal cooling time constant of

0.1 microsecond, thus, the thermite reactions can be quenched at different stages of reaction for ex-situ material characterizations. Through the time-resolved MTS diagnostics studies, we would gain the fundamental understanding of the dependence of thermite reaction kinetics on heating rates and the types of oxides used for the thermite mixtures.

In order to study the ignition and reaction mechanism of Al and their thermite mixtures with various oxidizers, we need to design a measurement system that can simultaneously meet the following criteria: 1) variable heating rates with the high heating rate capability (10^5 K/s or higher), 2) high cooling rates to quench reactions for ex-situ material characterization, and 3) a well-defined interface between the heater and testing materials. We recommend to use a micro-thermal stage (MTS) that meets all the above three criteria for the kinetic study of thermite reactions at variable heating rates and oxides.

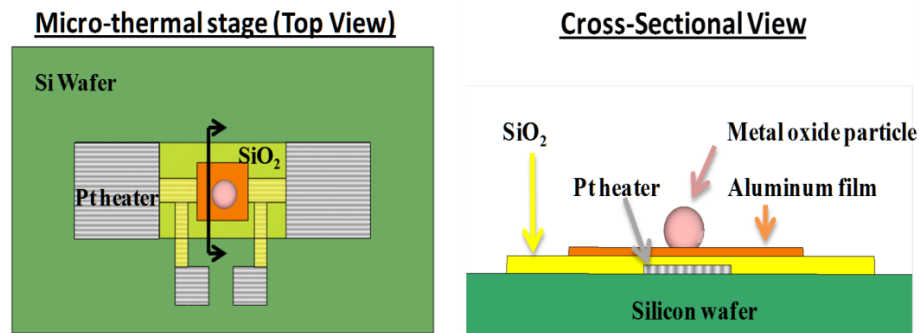


Figure 7-1: Experimental schematic of the micro-thermal stage

As shown in Figure 7-1, the MTS is composed of a micron scale Pt heater on a Si wafer. The planar thin film Pt heater is passivated (1 μm thick SiO_2) film for chemical and electrical insulation. The tested regions are located on top of the SiO_2 film where Al and thermite mixtures can be placed either as thin films or powders to control the interface between Al and oxides. The Pt heater generates heat by Joule heating that controls the temperature rise in the tested region. Due to the proximity between the Pt heater and the tested regions ($\sim 1\mu\text{m}$), the tested materials can be heated up rapidly with less than $1\mu\text{s}$ time delay. The temperature rise of the Pt heater can be precisely controlled by controlling the applied voltage amplitude and its heating rate is actively controlled by both the amplitude and pulse of the voltage. The heating rate of MTS can reach up to about 10^7 K/s, which is comparable to or potentially higher than the heating rate of 10^6 K/s reported for the T-jump [116] using a Pt wire (76 μm in diameter) and much higher than the heating rate of 10^3 K/s by the confined rapid thermolysis. [117] In addition, the Pt heater in MTS has a thin film geometry that can uniformly heat up the tested materials and enable testing both film and powder based energetic materials. The key of MST lies in the cooling rates. The cooling process of the Pt heater, no matter wire or film, is governed by the heat conduction process. The Pt wire is typically suspended in the air and the main cooling mechanism is governed by the heat conduction/convection process by air, but air has a very low thermal conductivity about 0.025 W/(mK) at room temperature. On the other hand, the Pt heater in MTS is located on top of a Si wafer and Si has a much higher thermal conductivity of 149 W/(mK) at room temperature so that it can remove heat much faster than air. The cooling rate of MTS is directly related to its thermal time constant that is defined as the time required for the Pt heater to lower its

temperature by 63.2% of a specific temperature span, i.e., from the max temperature of the Pt heater to room temperature. The thermal time constant of MTS is estimated to about 0.1 μ s. It should be noted that the thermal time constant of MTS can be tuned by varying the physical dimensions of different layers as well. The MTS has already been successfully applied to the measurement of the temperature and annealing dependence of the thermal properties of phase change materials, demonstrating a microsecond temporal resolution. It is logical to expect that MTS will have a similar positive impact on the study of rapid temperature heating and cooling of energetic materials, enabling fundamental understanding of their reaction kinetics.

7.2. Engineering application of flash ignition: Airbag igniter

The flash ignition research established within this thesis focused on understanding the mechanism of flash ignition and leads to future energetic device applications for improving the device performance (e.g., high ignition success rate, small ignition delay time, high energy release rate, etc.). A number of energetic applications for MEMS has been demonstrated, for examples airbag igniter [20], microthrusters [118], bonding [119], drug delivery [120], and micro-initiators [30, 121] using conventional ignition systems, such as hot wires, laser, and piezo-igniters. Very few studies have been reported to replace the ignition systems with xenon flash to demonstrate the feasibility of flash ignition and enhance their device performances. Among various energetic applications, the porous Si airbag igniter is the suitable energetic application that would benefit from the flash ignition since it requires a fast

and reliable ignition source. The airbag typically inflates within 20 - 30 msec to protect the driver and passenger from colliding into the steering wheel or dashboard. A high success rate of ignition is required; however, for small energetic applications, a large heat loss through the surrounding substrate becomes significant due to the large surface to volume ratio, which could lead to failure of ignition. There is a strong demand for the reliable ignition, for which the flash ignition could generate multi-point ignition sites to increase the reliability of ignition. Previous report has also proven that the multi-point ignition reduces the ignition delay time of hydrocarbon fuel [84], therefore, we expect that the flash ignition method would reduce the ignition delay time of porous Si resulting in a fast and stable inflation of the airbag.

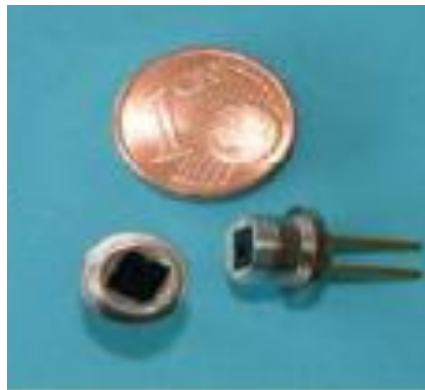


Figure 7-2: A prototype of a porous Si based airbag igniter. [20]

8. Bibliography

1. M. B. Talawar; R. Sivabalan; T. Mukundan; H. Muthurajan; A. K. Sikder; B. R. Gandhe; A. S. Rao, *Journal of hazardous materials* 161 (2-3) (2009) 589-607
2. R. A. Yetter, in: *2012 Princeton-CEFRC Summer School On Combustion*, Princeton University, 2012.
3. H. Y. Afeefy; J. F. Liebman; S. E. Stein, "Neutral Thermochemical Data" in NIST Chemistry WebBook, NIST Standard Reference Database Number 69, Eds. P.J. Linstrom and W.G. Mallard, National Institute of Standards and Technology, Gaithersburg MD, 20899, . <http://webbook.nist.gov>, (retrieved July 26, 2013),
4. S. H. Fischer; M. C. Grubelich, *Proceedings of 24th International Pyrotechnics Seminar*, Monterey, California, USA (1998)
5. M. W. Beckstead, *RTO/VKI special course on internal aerodynamics in solid rocket propulsion* (2002)
6. T. Bazyn; H. Krier; N. Glumac, *Proceedings of the Combustion Institute* 31 (2) (2007) 2021-2028
7. Y. Huang; G. A. Risha; V. Yang; R. A. Yetter, *Proceedings of the Combustion Institute* 31 (2) (2007) 2001-2009
8. M. A. Trunov; M. Schoenitz; E. L. Dreizin, *Propellants, Explosives, Pyrotechnics* 30 (1) (2005) 36-43
9. E. L. Dreizin, *Progress in Energy and Combustion Science* 35 (2) (2009) 141-167

10. M. A. Trunov; M. Schoenitz; E. L. Dreizin, *Combustion Theory and Modelling* 10 (4) (2006) 603-623
11. M. A. Trunov; M. Schoenitz; X. Zhu; E. L. Dreizin, *Combustion and Flame* 140 (4) (2005) 310-318
12. Y. Huang; G. A. Risha; V. Yang; R. A. Yetter, *Combustion and Flame* 156 (1) (2009) 5-13
13. V. I. Levitas; B. W. Asay; S. F. Son; M. Pantoya, *Journal of Applied Physics* 101 (8) (2007) 083524
14. V. I. Levitas; B. Dikici; M. L. Pantoya, *Combustion and Flame* 158 (7) (2011) 1413-1417
15. B. Dikici; S. W. Dean; M. L. Pantoya; V. I. Levitas; R. J. Jouet, *Energy & Fuels* 23 (9) (2009) 4231-4235
16. V. I. Levitas; M. L. Pantoya; K. W. Watson, *Applied Physics Letters* 92 (20) (2008) 201917
17. J. Gesner; M. L. Pantoya; V. I. Levitas, *Combustion and Flame* 159 (11) (2012) 3448-3453
18. M. C. G. S. H. Fischer, *Proc. 24th Int. Pyrotechnics Seminar, Monterey, CA* (1998) 1-6
19. L. J. Currano; W. A. Churaman, *Journal of Microelectromechanical Systems* 18 (4) (2009) 799-807

20. D. Clément; J. Diener; E. Gross; N. Künzner; V. Y. Timoshenko; D. Kovalev, *physica status solidi (a)* 202 (8) (2005) 1357-1364
21. C. Rossi; K. Zhang; D. Esteve; P. Alphonse; P. Tailhades; C. Vahlas, *Journal of Microelectromechanical Systems* 16 (4) (2007) 919-931
22. D. Kovalev; V. Timoshenko; N. Künzner; E. Gross; F. Koch, *Physical Review Letters* 87 (6) (2001)
23. E.-C. Koch; D. Clément, *Propellants, Explosives, Pyrotechnics* 32 (3) (2007) 205-212
24. A. Plummer; V. Kuznetsov; T. Joyner; J. Shapter; N. H. Voelcker, *Small* 7 (23) (2011) 3392-8
25. V. S. Parimi; S. A. Tadigadapa; R. A. Yetter, *Journal of Micromechanics and Microengineering* 22 (5) (2012) 055011
26. V. Simonenko; V. Zarko, *Energetic materials- Modelling of phenomena, experimental characterization, environmental engineering* (1999) 21-1
27. M. R. Weismiller; J. Y. Malchi; J. G. Lee; R. A. Yetter; T. J. Foley, *Proceedings of the Combustion Institute* 33 (2) (2011) 1989-1996
28. W. A. Churaman; L. J. Currano; C. J. Morris; J. E. Rajkowski; S. Bergbreiter, *Journal of Microelectromechanical Systems* 21 (1) (2012) 198-205
29. F. M. Dickey; W. A. Churaman; C. R. Becker; G. D. Metcalfe; B. M. Hanrahan; L. J. Currano; C. R. Stoldt; R. A. Beyer, *7795* (2010) 779506-779506-9
30. C. S. Staley; C. J. Morris; R. Thiruvengadathan; S. J. Apperson; K. Gangopadhyay; S. Gangopadhyay, *Journal of Micromechanics and Microengineering* 21 (11) (2011) 115015

31. C. J. Morris; K. E. Laflin; W. A. Churaman; C. R. Becker; L. J. Currano; D. H. Gracias, (2012) 1245-1248
32. E. L. Dreizin, Prog. Energ. Combust. 35 (2) (2009) 141-167
33. P. F. Pagoria; G. S. Lee; A. R. Mitchell; R. D. Schmidt, Thermochim Acta 384 (1-2) (2002) 187-204
34. M. B. Talawar; R. Sivabalan; T. Mukundan; H. Muthurajan; A. K. Sikder; B. R. Gandhe; A. S. Rao, J. Hazard. Mat. 161 (2-3) (2009) 589-607
35. R. A. Yetter; G. A. Risha; S. F. Son, Proc. Combust. Inst. 32 (2009) 1819-1838
36. D. Stamatis; Z. Jiang; V. Hoffmann; M. Schoenitz; E. Dreizin, Combust. Sci. Technol. 181 (1) (2009) 97-116
37. D. G. Kim; J. Kaneko; M. Sugamata, J. Jap. Inst. Metals 57 (11) (1993) 1325-1332
38. S. Umbrajkar; M. A. Trunov; M. Schoenitz; E. L. Dreizin; R. Broad, Propel. Expl. Pyrotech. 32 (1) (2007) 32-41
39. S. M. Umbrajkar; M. Schoenitz; E. L. Dreizin, Propel. Expl. Pyrotech. 31 (5) (2006) 382-389
40. M. Schoenitz; T. S. Ward; E. L. Dreizin, Proc. Combust. Inst. 30 (2005) 2071-2078
41. B. S. Bockmon; M. L. Pantoya; S. F. Son; B. W. Asay; J. T. Mang, J Appl Phys 98 (6) (2005) 064903/1-7
42. D. S. Moore; S. E. Son; B. W. Asay, Propel. Expl. Pyrotech. 29 (2) (2004) 106-111
43. K. B. Plantier; M. L. Pantoya; A. E. Gash, Combust. Flame 140 (4) (2005) 299-309

44. D. Prentice; M. L. Pantoya; B. J. Clapsaddle, J. Phys. Chem. B 109 (43) (2005) 20180-20185
45. R. Shende; S. Subramanian; S. Hasan; S. Apperson; R. Thiruvengadathan; K. Gangopadhyay; S. Gangopadhyay; P. Redner; D. Kapoor; S. Nicolich; W. Balas, Propel. Expl. Pyrotech. 33 (2) (2008) 122-130
46. S. Apperson; R. V. Shende; S. Subramanian; D. Tappmeyer; S. Gangopadhyay; Z. Chen; K. Gangopadhyay; P. Redner; S. Nicholich; D. Kapoor, Appl. Phys. Lett. 91 (24) (2007) 3
47. K. J. Blobaum; M. E. Reiss; J. M. P. Lawrence; T. P. Weihs, J Appl Phys 94 (5) (2003) 2915-2922
48. J. D. Ferguson; K. J. Buechler; A. W. Weimer; S. M. George, Powd. Technol. 156 (2-3) (2005) 154-163
49. V. E. Sanders; B. W. Asay; T. J. Foley; B. C. Tappan; A. N. Pacheco; S. F. Son, J. Prop. Pow. 23 (4) (2007) 707-714
50. K. J. Blobaum; A. J. Wagner; J. M. Plitzko; D. Van Heerden; D. H. Fairbrother; T. P. Weihs, Journal of Applied Physics 94 (5) (2003) 2923
51. K. Zhang; C. Rossi; G. A. A. Rodriguez; C. Tenailleau; P. Alphonse, Appl. Phys. Lett. 91 (11) (2007) 113117/1-3
52. K. L. Zhang; C. Rossi; M. Petrantoni; N. Maura, J. Microelectromech. S. 17 (4) (2008) 832-836

53. J. D. Ferguson; K. J. Buechler; A. W. Weimer; S. M. George, Powder Technology 156 (2-3) (2005) 154-163
54. C. R. Becker; S. Apperson; C. J. Morris; S. Gangopadhyay; L. J. Currano; W. A. Churaman; C. R. Stoldt, Nano letters 11 (2) (2011) 803-7
55. M. du Plessis, physica status solidi (c) 6 (7) (2009) 1763-1768
56. M. J. Sailor, Porous Silicon in Practice: Preparation, Characterization and Applications, Wiley-VCH Verlag GmbH & Co. KGaA, 2012
57. X. Jiang; T. Herricks; Y. Xia, Nano Lett. 2 (12) (2002) 1333-1338
58. V. I. Levitas; M. L. Pantoya; K. W. Watson, Applied Physics Letters 92 (20) (2008)
59. L. Wei; C. Hua, Journal of Alloys and Compounds 448 (1-2) (2008)
60. J. Y. Malchi; R. A. Yetter; T. J. Foley; S. F. Son, Combustion Science and Technology 180 (7) (2008) 1278-1294
61. R. Herino; G. Bomchil; K. Barla; C. Bertrand; J. L. Ginoux, Journal of The Electrochemical Society 134 (8A) (1987) 1994-2000
62. R. L. Smith; S. D. Collins, Journal of Applied Physics 71 (8) (1992) R1
63. J. M. Weisse; C. H. Lee; D. R. Kim; L. Cai; P. M. Rao; X. Zheng, (2013) Paper under review
64. R. Cisneros; H. Pfeiffer; C. Wang, Nanoscale Research Letters 5 (4) (2010) 686-691
65. M. Ghulinyan; C. J. Oton; G. Bonetti; Z. Gaburro; L. Pavesi, Journal of Applied Physics 93 (12) (2003) 9724

66. M. J. Sailor, Porous Silicon in Practice: Preparation, Characterization and Applications, Wiley-VCH Verlag GmbH & Co. KGaA, 2011
67. O. Kubaschewski; C. B. Alcock, Metallurgical Thermochemistry, Pergamon Press, London, 1979
68. S. M. Umbrajkar; M. Schoenitz; E. L. Dreizin, Thermochim Acta 451 (1-2) (2006) 34-43
69. A. Plummer; V. Kuznetsov; T. Joyner; J. Shapter; N. H. Voelcker, Small 7 (23) (2011) 3392-3398
70. N. A. Manesh; S. Basu; R. Kumar, Combustion and Flame 157 (3) (2010) 476-480
71. M. L. Pantoya; J. J. Granier, J. Therm. Anal. Calorim. 85 (1) (2006) 37-43
72. J. J. Granier; M. L. Pantoya, Combust. Flame 138 (4) (2004) 373-383
73. H. E. Kissinger, Anal. Chem. 29 (11) (1957) 1702-1706
74. C. Michaelsen; K. Barmak; T. P. Weihs, J. Phys. D-Appl. Phys. 30 (23) (1997) 3167-3186
75. M. W. Beckstead, Internal Aerodynamics in Solid Rocket Propulsion (2004) 1-46
76. C. J. T.P. Parr, D. Hanson-Parr, K. Higa, K. Wilson, 39th JANNAF Combustion Subcommittee Meeting (2003)
77. T. T. K. C.J. Bulian, J.A. Puszynski, 31st International Pyrotechnics Seminar, Fort Collins, CO (2004)

78. R. Shende; S. Subramanian; S. Hasan; S. Apperson; R. Thiruvengadathan; K. Gangopadhyay; S. Gangopadhyay; P. Redner; D. Kapoor; S. Nicolich; W. Balas, *Propellants, Explosives, Pyrotechnics* 33 (2) (2008) 122-130
79. C. Rossi; D. Estève, *Sensors and Actuators A: Physical* 120 (2) (2005) 297-310
80. P. M. Ajayan; M. Terrones; A. de la Guardia; V. Huc; N. Grobert; B. Q. Wei; H. Lezec; G. Ramanath; T. W. Ebbesen, *Science* 296 (5568) (2002) 705
81. N. Wang; B. D. Yao; Y. F. Chan; X. Y. Zhang, *Nano Letters* 3 (4) (2003) 475-477
82. L. J. Cote; R. Cruz-Silva; J. X. Huang, *Journal of the American Chemical Society* 131 (31) (2009) 11027-11032
83. M. R. Manaa; A. R. Mitchell; R. G. Garza; P. F. Pagoria; B. E. Watkins, *Journal of the American Chemical Society* 127 (40) (2005) 13786-13787
84. A. M. Berkowitz; M. A. Oehlschlaeger, *Proceedings of the Combustion Institute* 33 (2) (2011) 3359-3366
85. J. L. Prentice, *Combustion Science and Technology* 1 (5) (1970) 385-398
86. H. K. Aslin, *Review of Scientific Instruments* 38 (3) (1967) 377
87. N. Zeng; A. B. Murphy, *Nanotechnology* 20 (37) (2009) 375702
88. Y. A. Akimov; W. S. Koh, *Nanotechnology* 21 (23) (2010) 235201
89. H. H. Richardson; M. T. Carlson; P. J. Tandler; P. Hernandez; A. O. Govorov, *Nano Letters* 9 (3) (2009) 1139-1146

90. D. G. Cahill; W. K. Ford; K. E. Goodson; G. D. Mahan; A. Majumdar; H. J. Maris; R. Merlin; S. R. Phillpot, *Journal of Applied Physics* 93 (2) (2003) 793-818
91. P. Laven, MiePlot v4.2 software is available at www.philiplaven.com/MiePlot.htm
92. M. A. Trunov; M. Schoenitz; E. L. Dreizin, *Propellants Explosives Pyrotechnics* 30 (1) (2005) 36-43
93. E. L. Dreizin, *Prog. in Energy Combust. Sci.* 35 (2) (2009) 141-167
94. R. A. Yetter; G. A. Risha; S. F. Son, *Proceedings of the Combustion Institute* 32 (2009) 1819-1838
95. A. O. Govorov; H. H. Richardson, *Nano Today* 2 (1) (2007) 30-38
96. B. Lewis; G. Von Elbe, in: *Combustion, flames and explosions of gases*, Academic Press: New York, 1987
97. Y. Yang; Z. Sun; S. Wang; D. D. Dlott, *The Journal of Physical Chemistry B* 107 (19) (2003) 4485-4493
98. E. V. Chernenko; L. F. Afanaseva; V. A. Lebedeva; V. I. Rozenband, *Combust Explo Shock+* 24 (6) (1988) 639-646
99. C. F. Bohren; D. R. Huffman, in: *Absorption and Scattering of Light by Small Particles*, Wiley-VCH Verlag GmbH: Weinheim, Germany, 1998
100. S. Kaierle; S. Wang; R. Shen; Y. Ye; Y. Hu; L. Wu; C. Yang; J. Liu; J. Cao, 8796 (2013) 87960C-87960C-6
101. S. Wang; R. Shen; Y. Ye; Y. Hu, *Nanotechnology* 23 (43) (2012) 435701

102. M. R. Manaa; A. R. Mitchell; R. G. Garza; P. F. Pagoria; B. E. Watkins, *Journal of the American Chemical Society* 127 (40) (2005) 13786-7
103. N. Wang; B. D. Yao; Y. F. Chan; X. Y. Zhang, *Nano letters* 3 (4) (2003) 475-477
104. Y. Ohkura; P. M. Rao; I. S. Cho; X. Zheng, *Applied Physics Letters* 102 (4) (2013) 043108
105. Y. Ohkura; P. M. Rao; X. Zheng, *Combustion and Flame* 158 (12) (2011) 2544-2548
106. A. G. Cullis; L. T. Canham, *Nature* 353 (6342) (1991) 335-338
107. G. Amato, *Optical Engineering* 36 (2) (1997) 423
108. J. M. Devi; M. Jeyachandran; K. Ramachandran, *e-Journal of Nondestructive Testing and Ultrasonics* 11 (6) (2006)
109. Q. Shen; T. Toyoda, *Review of Scientific Instruments* 74 (1) (2003) 601
110. V. Torres-Costa; R. J. Martín-Palma, *Journal of Materials Science* 45 (11) (2010) 2823-2838
111. R. S. Dubey; D. K. Gautam, *Journal of Optoelectronic and Biomedical Materials* 1 (1) (2009) 8-14
112. R. H. Perry; D. W. Green, *Perry's Chemical Engineers' Handbook*, McGraw-Hill Professional Publishing, 1984
113. H. Diesinger; A. Bsiesy; R. Hérino, *Journal of Applied Physics* 89 (1) (2001) 221
114. D. Kovalev; G. Polisski; M. Ben-Chorin; J. Diener; F. Koch, *Journal of Applied Physics* 80 (10) (1996) 5978

115. S. Datta; K. Narasimhan, *Physical Review B* 60 (11) (1999) 8246-8252
116. K. T. Sullivan; N. W. Piekiet; C. Wu; S. Chowdhury; S. T. Kelly; T. C. Hufnagel; K. Fezzaa; M. R. Zachariah, *Combustion and Flame* 159 (1) (2012) 2-15
117. M. R. Weismiller; S. Q. Wang; A. Chowdhury; S. T. Thynell; R. A. Yetter, *Thermochimica Acta* 551 (2013) 110-117
118. K. L. Zhang; S. K. Chou; S. S. Ang; X. S. Tang, *Sensors and Actuators A: Physical* 122 (1) (2005) 113-123
119. J. Matteau in: *NanoBond Assembly - A Rapid, Room Temperature Soldering Process*, 5th International Brazing and Soldering Conference, Las Vegas Nevada, 2012; Las Vegas Nevada, 2012.
120. C. S. Staley, Development of nanoenergetic micro-fluidic jet injectors, Army Research Laboratory, Adelphi, MD, 2012
121. C. Cane; P. Pennarun; C. Rossi; D. Esteve; V. Conedera; J.-C. Chiao; F. Vidal Verdu, 5836 (2005) 558-569